Science and Technology Indonesia
e-ISSN:2580-4391 *p*-ISSN:2580-4405
Vol. 11, No. 2, April 2026

Research Paper

Preparation of Polyacrylonitrile-Polyethersulfone Nanofibers Loaded with Reduced Graphene Oxide from Palm Kernel Shell for Wastewater Filtration

Rahma Dani[1,2], Muhammad Rama Almafie[2,3], Agung Mataram[4], M. Danny Pratama Lamura[5], Hamdi Akhsan[1], Leni Marlina[1], Ahmad Fudholi[6], Ahmad Fauzi Ismail[7], Ida Sriyanti[1,2*]

[1]*Department of Physics Education, Faculty of Teacher Training and Education, Universitas Sriwijaya, South Sumatra, 30662, Indonesia*
[2]*Instrumentation, Material, Computation Research Group, Universitas Sriwijaya, Palembang, South Sumatra, 30139, Indonesia*
[3]*Doctoral of Mathematics and Natural Sciences, Faculty of Mathematics and Natural Sciences, Universitas Sriwijaya, South Sumatra, 30662, Indonesia*
[4]*Department of Mechanical Engineering, Faculty of Engineering, Universitas Sriwijaya, South Sumatra, 30662, Indonesia*
[5]*Department of Mechanical Engineering, Faculty of Engineering and Science, Universitas Pembangunan Nasional Veteran Jawa Timur, Surabaya, East Java, 60294, Indonesia*
[6]*Research Center for Energy Conversion and Conservation, National Research and Innovation Agency (BRIN), South Tangerang, 15314, Indonesia*
[7]*Advanced Membrane Technology Research Centre (AMTEC), Faculty of Chemical and Energy Engineering, Universiti Teknologi Malaysia, Skudai, Johor, 81310, Malaysia*
***Corresponding author**: ida_sriyanti@unsri.ac.id

Abstract
The development of Polyacrylonitrile (PAN)–Polyethersulfone (PES) nanofiber membranes loaded with Reduced Graphene Oxide (rGO) offers an innovative and sustainable solution for water filtration. This study synthesized and characterized PAN–PES loaded rGO nanofiber membranes using an electrospinning technique. A PAN–PES mixture (8:2 mass ratio) at 10–20 wt% served as the matrix, with 48 mg of rGO added. The membranes were analyzed using scanning electron microscopy, Fourier-transform infrared spectroscopy (FTIR), X-ray diffraction (XRD), mechanical testing, water absorption, immersion resistance, and clean water permeability (CWP). The resulting nanofibers exhibited defect-free, bead-free, and uniform morphology with diameters ranging from 389 to 757 nm. FTIR confirmed hydrogen bonding between PAN–PES and rGO, while XRD showed sharp peaks with a maximum crystallinity of 33.52%. The membrane displayed a Young's modulus of 57.83 MPa and remained stable after 32 days of immersion. It demonstrated superhydrophilic behavior with a contact angle of 72.4° to 74.3°, sustaining a stable water flux at 6.0 bar for 60 min, yielding a permeability of 3.25 to 23 L/m^2·h·bar and an equilibrium water content of 69 to 91%. Surface morphology before and after wastewater filtration revealed effective contaminant capture and strong antifouling resistance. These results confirm that PAN–PES loaded rGO nanofiber membranes possess excellent mechanical stability, high permeability, and superior wettability, providing a promising pathway for advanced, sustainable water filtration applications.

Keywords
Absorption, Membrane, Permeability, Resistance, Wettability

Received: 8 November 2025, Accepted: 24 January 2026
https://doi.org/10.26554/sti.2026.11.2.457-480

1. INTRODUCTION

The availability of clean water is increasingly threatened due to rising pollution loads from industrial and domestic activities in various countries, including Indonesia. One clear indicator of water quality degradation is the change in river color to yellowish (Rangecroft et al., 2023). One clear indicator of water quality degradation is a change in the river's color to yellowish. This color is generally caused by high levels of dissolved organic matter such as tannins and lignin originating from biomass waste, as well as the presence of heavy metals like iron and chromium produced by the textile, pulp and paper, and mining industries. The presence of these compounds not only causes color changes, but also indicates the existence of pollutants that are difficult to degrade naturally and can be toxic to aquatic organisms. Various conventional methods such as coagulation, flocculation, and adsorption have been used to treat colored wastewater, but their effectiveness is often limited against nano- and micro-sized contaminants. In addition, these processes can produce secondary chemical residues that have the potential to pollute the environment. In the past two decades, membrane-based separation technologies have emerged as a promising alternative because they are able to physically remove contaminants with high efficiency and without generating hazardous by-products (Zhao et al., 2024). Nevertheless, conventional flat-sheet membranes often face challenges such as fouling

and low water permeability. To overcome these issues, the development of nanofiber membranes produced through the electrospinning method is receiving increasing attention. The nanofiber structure offers a high specific surface area, uniform pore distribution, and better water permeability compared to conventional membranes (Wang et al., 2025). The next challenge is selecting base materials that have an optimal balance of mechanical, chemical, and surface properties to maximize wastewater filtration performance.

Among various synthetic polymers, Polyacrylonitrile (PAN) and Polyethersulfone (PES) are two materials that are widely used for membrane fabrication due to their good chemical, thermal, and mechanical stability. PAN is capable of stably forming fibers with nanoscale diameters through electrospinning, and it is easily chemically modified because it contains reactive nitrile groups. Research on the development of nanofiber membranes for water filtration has been extensively conducted by previous researchers. Roche and Yalcinkaya (2019) reported a water permeability value of 600 $L.m^{-2}.h^{-1}.bar^{-1}$ for pure PAN membranes. Meanwhile, Jang et al. (2020) reported a value of 390 $L.m^{-2}.h^{-1}.bar^{-1}$ for the Ag/GO composite-modified PAN membrane. Meanwhile, PES is known for its mechanical strength and resistance to organic solvents, but its relatively hydrophobic nature often leads to fouling. The combination of PAN and PES in a single polymer matrix can produce a synergistic effect, where PAN enhances hydrophilicity and permeability, while PES reinforces mechanical stability and chemical resistance. Meanwhile, Pervez et al. (2022) reported that the PES/PAN mixed membrane has mechanical stability and hydrophilicity (contact angle 65.9 ± 1.2°) which will affect its absorption capacity, namely MB (1010 mgMB/g), which is better than that of the pure membrane (48 mg/g). Previous studies have also shown that membrane performance can be further enhanced by the addition of nanomaterials such as graphene oxide (GO) or reduced graphene oxide (rGO), which serve as structural reinforcements and improve hydrophilicity. Therefore, the combination of PAN–PES with rGO filler becomes a promising approach to produce nanofiber membranes with high filtration performance.

Reduced Graphene Oxide (rGO) is a two-dimensional carbon-based material that possesses exceptional mechanical properties, a high surface area, as well as good electrical and thermal conductivity (Manikandan and Lee, 2023). In the context of filtration membranes, rGO plays an important role in forming water transport channels through parallel-aligned graphene layers, thereby reducing diffusion resistance and increasing permeability. Motlokoa et al. (2025) reported that the addition of 1 to 5 wt% rGO to PES membranes increased water flux (38 $L\,m^{-2}h.^{-1}.bar^{-1}$), whereas Rostami et al. (2024) showed that the addition of GO increased permeability by 80% and selectivity by 76% for heavy metal ions such as Pb. Compared to GO, rGO has a lower oxygen content, making it structurally more stable and less prone to swelling in aqueous media (Liu et al., 2022). However, the dispersion of rGO within the polymer matrix often becomes a challenge due to its tendency to agglomerate. Therefore, various approaches such as surface modification of rGO and optimization of the filler ratio have been employed to ensure even distribution and strong bonding with the polymer matrix. The incorporation of rGO with the PAN–PES system is expected to enhance water permeability, as well as provide improved antifouling capabilities and mechanical strength compared to conventional membranes (Edokali et al., 2024). Although a number of studies have explored the use of synthetic GO/rGO based on commercial graphite, sustainable and low-cost sources of rGO from biomass have still rarely been developed.

One of the most promising sources of biomass is Palm Kernel Shell (PKS), a solid waste product from palm oil processing that is abundant in Indonesia and other tropical countries (Nabila et al., 2023). PKS contains a high carbon content (around 48–52%) and can be used as a raw material to produce graphene oxide or reduced graphene oxide through carbonization and chemical reduction processes. The utilization of PKS can add value to agricultural waste and support the principles of the circular economy in the field of materials. Faaizatunnisa et al. (2025) used ZnO/rGO nanocomposites derived from PKS via a modified Hummers method, showing an increase in surface area and adsorption capacity, achieving 95% degradation of 2-naphthol after 120 minutes of irradiation, surpassing pure ZnO. Mohd Ali Jinnah et al. (2024) successfully synthesized rGO from PKS using a double oxidation and carbonization method, achieving a Rhodamine B adsorption efficiency of up to 195.24 mg/g. Meanwhile, Ab Aziz et al. (2023) have successfully synthesized rGO using the same method from PKS, with a maximum adsorption capacity reaching 50.07 mg/g. These results indicate that PKS-based rGO has characteristics similar to commercial rGO in terms of adsorption capacity and hydrophilicity. However, the use of rGO from PKS as a filler in PAN–PES nanofibers for wastewater filtration applications has not been widely reported. This combination of sustainable materials has great potential to produce environmentally friendly membranes with high performance (Adhikary and Goswami, 2025). In addition to reducing dependence on fossil carbon sources, the integration of rGO-PKS can improve the porosity and structural stability of nanofibers, as well as enhance the membrane's ability to remove organic and inorganic contaminants from wastewater.

Research on the development of nanofiber membranes for water filtration has been extensively conducted by previous researchers. Chen et al. (2022) reported a water permeability value of 8490 $L.m^{-2}.h^{-1}.bar^{-1}$ for PAN/TPU composite nanofiber membranes. Meanwhile, Askari et al. (2024) reported a value of 1265 $L.m^{-2}.h^{-1}.bar^{-1}$ for PES/PAN membranes in oil/water separation applications, with an oil separation efficiency reaching 86%. Another study by Elessawy et al. (2024) also reported that the addition of graphene oxide (GO) into the PES nanofiber matrix was able to increase water permeability up to 1367 LMH, with a maximum rejection rate of around 93%, as well as enhanced membrane hydrophilicity and porosity. Meanwhile, Liu et al. (2023) reported that the combi-

nation of PAN/PES/TiO_2 resulted in an increase in water flux up to 619.4 L/m^2·h·bar, as well as demonstrating better fouling resistance compared to single membranes. Lastly, Ebrahimi et al. (2022) developed a PAN/GO/SiO2 membrane, which demonstrated oil/water separation with a 98% rejection rate, confirming that the integration of carbon-based materials can significantly enhance filtration performance. However, there have not been many studies that integrate biomass-based rGO, especially those derived from Palm Kernel Shell (PKS), into PAN–PES composites for wastewater filtration applications, systematically investigating the influence of electrospinning process parameters on filtration performance using statistical approaches such as Response Surface Methodology, as well as combining approaches of material synthesis, membrane fabrication, and filtration performance optimization within an integrated research framework.

This research explores the utilization of Palm Kernel Shell (PKS) as a natural carbon source for the synthesis of reduced graphene oxide (rGO) and its application as a filler material in PAN-PES nanofiber composites for water filtration applications. This approach provides a biomass-based alternative that has the potential to support sustainability and local waste utilization. The combination of PAN-PES with PKS-based rGO is still relatively limited reported in the wastewater filtration literature, so this study contributes to expanding the understanding of the effect of biomass-based rGO on structural properties and membrane filtration performance. This research was conducted through an integrated experimental approach that includes material synthesis, nanofiber fabrication, characterization, and filtration performance evaluation. Material characterization was carried out using various techniques, such as SEM and TEM for morphological analysis, FTIR for functional group identification, XRD for crystal structure analysis, and contact angle measurement to evaluate the hydrophilicity level of the membrane. In addition, direct testing was also conducted on the nanofiber surface morphology before and after the wastewater filtration process to observe structural changes and fouling potential on the membrane surface. The membrane's performance in the filtration process was evaluated through absorption capacity testing and clean water permeability testing to assess separation efficiency as well as fluid transport characteristics. Thus, this research is expected to provide both scientific and practical contributions to the development of sustainable nanofiber membrane technology for industrial wastewater treatment in the future.

2. EXPERIMENTAL SECTION

2.1 Materials

In this study, Polyacrylonitrile (PAN, CAS 25014-41-9) was obtained from Sigma Aldrich Co., Ltd. (Singapore) and a molecular weight of 150,000 g/mol. Polyethersulfone (PES, SU306311) granules with a nominal granule size of 3 mm, weight of 200 g, and clear amber color were purchased from Sigma Aldrich Co., Ltd. (Singapore) with a molecular weight of 64,000 g/mol. N, N-dimethylformamide (DMF, anhydrous, 99.8%, CAS No. 68-12-2) was obtained from Sigma-Aldrich Co (Singapore). Reduced Graphene Oxide (rGO) was synthesized from Palm Kernel Shells (CKS) using a hydrothermal method, as previously described (Jauhari et al., 2021; Widiatmoko et al., 2019). Other materials and reagents were used directly without further modification, unless otherwise stated.

2.2 Fabrications of Nanofiber Membranes

Figure 1 illustrates the manufacturing process of the PAN-PES loaded rGOPKS electrospun nanofiber membrane. In this experiment, a PAN-PES polymer with a mass ratio of 8:2 was used as the matrix at concentrations of 10, 15, and 30 wt.%, dissolved homogeneously in the organic solvent DMF (90 wt.%) using magnetic stirring (Thermo Scientific Cimarec, USA) at a temperature of 80°C for 12 hours. rGOPKS (48 mg) was added and mixed with vigorous stirring at 300 rpm and 80°C for 8 h. The compositions of the polymer solutions are summarized in Table 1. The NLI603 electrospinning facility was supplied by Nanolab Instruments Sdn. Bhd. The PAN-PES loaded rGOPKS dope solution was placed into a 10 cc/mL plastic syringe (Terumo-Syring®, Indonesia) connected to a stainless-steel needle (outer diameter 0.8 mm). The needle was connected to the positive terminal of the voltage generator. A working voltage of 15 kV and a flow rate of 1.5 ml/h (through an injection pump controlled by a human-machine interface touchscreen) were used. The environmental parameters were maintained at a room temperature of 30°C and relative humidity of approximately 60%. The successful preparation of electrospun nanofibers was confirmed by observing the Taylor cone, and finally, the nanofiber mats were collected onto a nonwoven fabric placed 100 cm from the needle tip. The resulting PAN-PES loaded rGOPKS nanofiber membrane was separated from the nonwoven sheet. The entire experimental process was completed in 3 h. The fiber membranes were placed in a vacuum drying oven at 40°C for 24 h to remove residual organic solvents.

Table 1. Composition of the Polymer Solution for Substrate Preparation

Sample	PAN-PES (8:2 wt.%)	rGOPKS (mg)
PAN-PES	10	0
PPG10	10	48
PPG15	15	48
PPG20	20	48

2.3 Methods of Characterization

2.3.1 Morphology of rGOPKS

Observation morphologies were performed to reduction Graphene Oxide of Palm Kernel Shell (rGOPKS). The morphology and size of rGOPKS were investigated by scanning electron microscopy (SEM, TESCAN-Vega 3, Czech Republic) after coating with a 10 nm gold layer. The surface morphology of rGOKS was observed using a Tecnai G2 20S-TwinTransmission Electron Microscopy (FEI., USA) at a voltage of 100 kV.

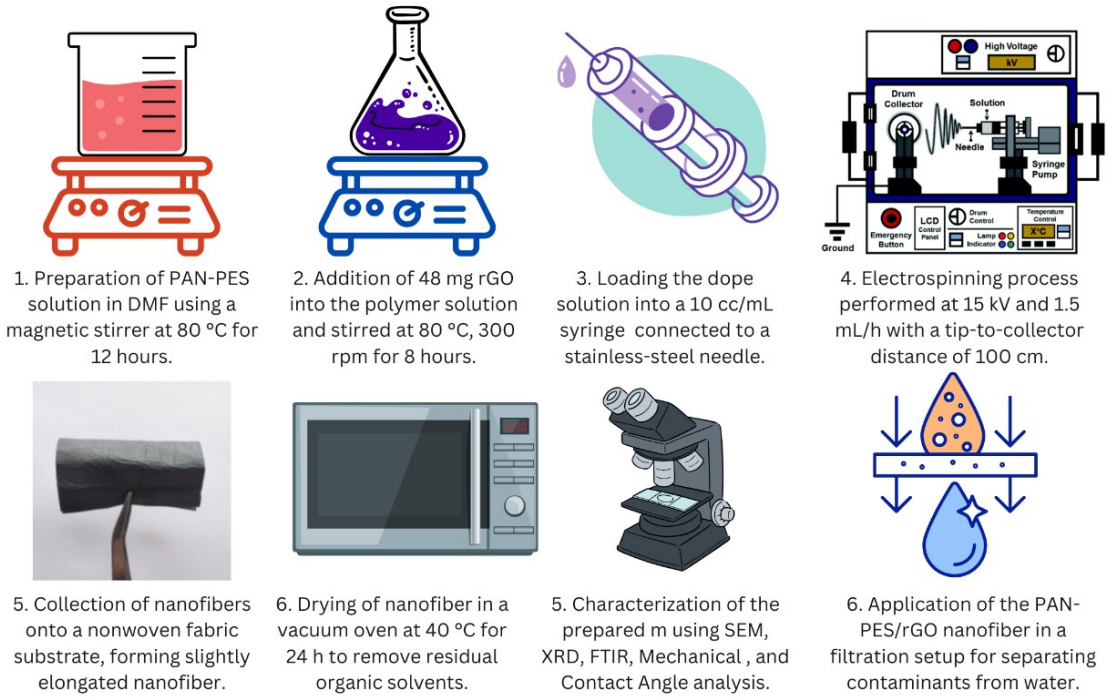

Figure 1. Schematic Illustration of the Preparation, Fabrication, and Application of the PAN–PES/GOPKS Electrospun Nanofiber Membrane

2.3.2 Morphology of Electrospun Nanofibers

The morphology of the electrospun nanofibers was investigated using field-emission scanning electron microscopy (SEM) (JEOL JSM 6510 LA, Japan) with an accelerating voltage of 20 kV and a working distance of 20 mm. Samples were prepared by loading electrospun PAN-PES loaded rGOPKS onto carbon tape on an aluminum disk. The samples were gold sputtered and then loaded into the SEM sample chamber for analysis. The diameters of 100 fibers were determined using ImageJ software (National Institute of Health, USA) in the SEM image, and the diameter distribution was calculated.

2.3.3 FTIR and XRD Analysis

Fourier-transform infrared (FT-IR) spectroscopic measurements of the as-prepared PAN-PES loaded rGOPKS composite nanofibers were performed on an IR spectrophotometer (Nicolet iS50, Thermo Scientific, USA) in the scanning range from 4000 to 400 cm^{-1}. X-Ray Diffraction (XRD, Bruker D2 Phaser) patterns were recorded from 10° to 90° with a step size of 0.03° using Cu-Kα photons (λ = 1.5406 Å) to analyze the structural details of the carbonized pristine and modified nanofibers. The interlayer spacing, d, was calculated using Bragg's law (Equation 1), where θ is the Bragg angle. The crystallite sizes were estimated using the Scherrer equation (Equation 2), as follows: where λ is the X-ray wavelength, n was set as 1, K is the shape factor (0.89 for L_c), β is the full width at half maximum (FWHM) of the diffraction peak, and θ the Bragg angle in radians. The relative percentage of crystallinity was determined by dividing the total area of the crystal peaks by the total area (total intensity) of the spectrum. The relative percentage of crystallinity (X_c%) was then calculated using the ratio of these two intensities, as shown in Equation 3, where I_c = total intensity of the crystalline peaks and I_a = total intensity of the amorphous peak (Almafie et al., 2025; Sriyanti et al., 2025, 2026).

$$d = \frac{n\lambda}{2\sin\theta} \tag{1}$$

$$L = \frac{K\lambda}{\beta\cos\theta} \tag{2}$$

$$\chi_c(\%) = \frac{I_c}{I_c + I_a} \tag{3}$$

2.3.4 Mechanical Properties

Tensile tests were performed to determine the mechanical properties of the composite. Universal Tensile Strength Testing Machine (ZwickRoell, BT2-FR020TH. A60 (Germany)

was used to conduct tensile tests following ASTM standard D3039/D3039M to assess the mechanical properties of the fabrics at room temperature. The test specimens were three pieces, each 1 cm wide and 2 cm long. The distance between the fixtures was 2 cm. The load cell was 100 cN, the extension rate was 0.6 mm/min, and the gauge length was 10 mm. The data obtained from the tensile tests, maximum stress (UTS), elongation, and Young's modulus values of the composite specimens were determined.

2.3.5 Water Contact Angle

The surface wettability of the modified membranes was examined using a Digital Microscope (Model X4, Magnification 1600×). This instrument facilitated the measurement of the angle formed between a liquid droplet and the surface of the modified membranes, which served as an indicator of surface hydrophilicity or hydrophobicity. The nanofibers were stuck on glass slides, and a drop of Milli-Q water (3 μL) was applied to the film surface. The drop images were captured using a digital camera. Subsequently, the contact angle values from 0 to 50 min were measured using ImageJ software. The mean value of the contact angle was calculated from three individual tests performed at different positions on the nanofibers.

2.3.6 Water Absorption Test

The wettability of a material is largely dependent on its hydrophilic and hydrophobic nature. Therefore, this study investigated whether the hygroscopicity of the prepared nanocomposite film met the requirements for water filtration by testing the hygroscopicity and equilibrium water content of the material. To test the water absorption by the nanofiber membrane, the prepared nanofiber membrane was cut into small pieces of size $20 \times 20\,mm^2$ with mass m_0. Second, the samples were immersed in 10 mL of deionized water at 37 °C for 2 h, then removed, and the excess deionized water was gently wiped off the surface with filter paper and weighed as m_t. The absorption rate and equilibrium water content of the fibres membrane were calculated using Equation 4 and Equation 5, respectively (Hou et al., 2023; Shahryari et al., 2021).

$$\text{Absorption rate (\%)} = \frac{m_t - m_0}{m_t} \times 100\% \quad (4)$$

$$\text{Equilibrium water content (\%)} = \frac{m_t - m_0}{m_t} \times 100\% \quad (5)$$

2.3.7 Water Resistance

To test the nanofiber degradation in liquids, a test solution was prepared. This solution was suitable for testing. The nanofiber samples were cut into uniform sizes of $20 \times 20\ mm^2$. The sample was placed in a container containing the test solution and was completely submerged. The container was tightly sealed and incubated at room temperature (35 °C) to simulate the actual water filtration conditions. At certain time intervals (1, 8, 16, 24, and 32 days), samples were collected for further analysis. During the test, any visual changes in the nanofibers, such as changes in texture, shape, or color, were observed and recorded. The process was repeated with multiple replicates to ensure accuracy.

2.3.8 Water Permeability

The performance of the membrane water filter was determined by the normalized clean water permeability (CWP, Indonesia) using a cassette cleanliness test. This involves measuring the flow of clean water through the membrane at a standard pressure and temperature. The membrane was wetted in ultrapure water for a maximum of 60 min, pumped to a pressure of 2.0 – 6.0 bar, and its performance was measured. The Water Flux of the nanofiber membrane was calculated using Equation 6 (Mataram et al., 2024). where Jv is the volumetric flux, expressed in units of liters per square meter per hour per bar. V is the volume of permeate produced during the filtration process (L), A is the effective surface area of the membrane used (m^2), t is the operating time (hours), and P indicates the applied operating pressure (bar).

$$J_v\ (\mathrm{L\,m^{-2}\,h^{-1}\,bar^{-1}}) = \frac{V}{A\,t\,P} \quad (6)$$

2.3.9 Wastewater Filtration Test

The wastewater filtration performance of PAN-PES nanofiber membranes containing reduced graphene oxide derived from palm kernel shell (rGOPKS) was evaluated using a simple gravity-driven setup (Figure 12a). The filtration device was constructed from a modified plastic bottle and a glass beaker, with the nanofiber membrane securely positioned between them as the active filtration layer. Wastewater samples were collected from the Ogan River in Muara Penimbung Ilir Village, Indralaya, Ogan Ilir, South Sumatra, Indonesia, characterized by high turbidity and suspended solids. Approximately 100 mL of raw water was poured into the upper chamber and allowed to pass through the membrane under atmospheric pressure (1 atm) at room temperature (±27°C) without any external force applied. The membranes were visually examined before and after filtration to observe color and surface changes (Figure b and 10d). Morphological analysis was conducted using scanning electron microscopy (SEM) to evaluate fiber structure and the presence of residual impurities.

2.3.10 Statistical Analysis

Statistical analysis was performed using OriginLab software. The data were analyzed using one-way ANOVA followed by Tukey's HSD post-hoc test to determine statistically significant differences at a significance level of $p < 0.05$. All data are presented as Mean ± standard deviation (SD).

3. RESULTS AND DISCUSSION

3.1 Analysis Morphology of rGOPKS Using SEM and TEM

Figure 2 shows the results of surface morphology characterization of rGOPKS (reduced Graphene Oxide from Palm Oil

Kernel Shell) using Scanning Electron Microscopy (SEM) at two magnification levels. rGOPKS was synthesized through the pyrolysis process of POKS at temperatures of 700–900°C with the aid of an $FeCl_3$ catalyst. During this process, Fe^{3+} ions in $FeCl_3$ are reduced to Fe^o, which acts as a nucleation center where carbon atoms diffuse and form a graphitic structure (Zakaria et al., 2024). As the pyrolysis temperature increases, carbon atoms from the biomass are directed to form graphene layers, which are then oxidized into graphene oxide (GOPKS) and subsequently reduced to rGOPKS. This phenomenon is consistent with the findings of Widiatmoko et al. (2019), who reported that activated carbon from palm fruit can transform into graphene as the pyrolysis temperature rises from 700°C to 800°C (Widiatmoko et al., 2019). The SEM image at low magnification (Figure 2a) shows that the sample consists of aggregates of thin sheets stacked irregularly, forming a porous and layered structure. At higher magnification (Figure 2b), it can be seen that the edges of the rGOPKS sheets are irregular and the surfaces are wavy. This corrugated morphology is caused by the bending of the two-dimensional sheets, resulting in thermodynamically stable rumpled structures. This structure increases the active surface area and enhances the number of adsorption sites for pollutants such as heavy metal ions and organic compounds. Several studies support these findings. Alimohammady et al. (2025) reported that graphene oxide-based 5-ATP-GO has high adsorption capacity and selectivity for Cd(II), Hg(II), and As(III) ions. Ristiani et al. (2022) reported that increasing the heating temperature of graphene-based carbon from coconut shells produces a mixed 2D–3D structure with meso- and microporous morphology. Meanwhile, Davidová et al. (2024) reported that the pyrolysis of montmorillonite with low molecular weight carbon sources produces conductive materials containing graphite and multilayer graphene, with conductivity reaching up to 35 S m^{-1}. These results reinforce that the process of forming rGOPKS from Palm Oil Kernel Shell through high-temperature pyrolysis and $FeCl_3$ reduction is effective in producing a water filtration material with active morphology and a high surface area.

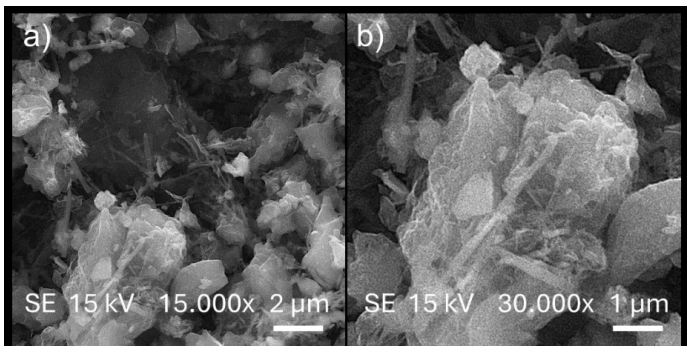

Figure 2. Scanning Electron Microscopy Images of the rGOPKS Sample at Two Magnifications: (a) 15,000× with a Scale Bar of 2 μm, and (b) 30,000× with a Scale Zar of 1 μm

Figure 3 shows the results of TEM characterization of rGOPKS samples at various magnifications as well as selected area electron diffraction (SAED) patterns. In the low magnification TEM image (Figure 3a), it can be seen that the sample consists of aggregates of thin sheets with relatively large lateral sizes, indicating that the rGOPKS structure still retains the characteristic morphology of graphene-based materials. These sheets appear to cover most of the TEM grid area, indicating good particle dispersion in the colloidal suspension (Vella et al., 2025). An HR-TEM image at medium magnification (Figure 3b) shows in greater detail the geometric shapes of the edges of the sheets. It can be observed that the rGOPKS flakes have relatively regular edges and do not show any significant signs of damage on the basal plane, indicating that the reduction process and composite formation do not cause severe structural degradation (Utkan et al., 2023). At high magnification (Figure 3c), several layers of rGOPKS stacked on top of each other can be clearly seen. The lattice fringe patterns indicate interlayer distances consistent with a partially reduced graphitic structure, where the layers' orientations are not completely parallel, possibly due to random overlap (turbostratic stacking) resulting from the exfoliation and reduction processes (Joshi et al., 2024). The Selected Area Electron Diffraction (SAED) pattern in Figure 3d shows faint diffraction rings with weak, unevenly distributed spots, indicating that the rGOPKS material has semi-crystalline properties. The presence of diffuse patterns with low intensity suggests that some graphitic domains have been restored during the reduction process, while others remain in the amorphous phase due to residual oxygen functional groups and structural defects (Schuepfer et al., 2020). This feature is a distinctive characteristic of reduced graphene oxide (rGO), where the reduction process only restores part of the sp^2 bonds in the carbon framework, resulting in a combination of orderly graphitic regions and amorphous regions as a consequencide of the partial reduction of graphene oxide (Rapisarda et al., 2020). This reinforces the conclusion that rGOPKS material has a semi-crystalline structure, consistent with the partial reduction of graphene oxide resulting in a combination of ordered graphitic regions and disordered regions due to structural defects.

3.2 PAN-PES loaded rGOPKS Nanofiber

Figure 4 highlights the notable visual distinction between the pure PAN-PES solution and the PAN-PES solution loaded with rGOPKS. The pure PAN-PES solution was clear, signifying a uniform distribution of the two polymers, polyacrylonitrile (PAN) and polyethersulfone (PES) is show in Figure 4a. However, when rGOPKS, which is inherently deep black, is added, the PAN-PES solution darkens upon homogeneous mixing, as observed in samples PPG10, PPG15, and PPG20. This color transformation is attributed to rGOPKS high light absorption of rGOPKS, which stems from its extensive sp^2 hybrid structure (Sabet and Soleimani, 2022). Idjan et al. (2025) reported that mixing PVA/CA with yellow wood extract produces yellowish fibers due to natural chromophoric compounds.

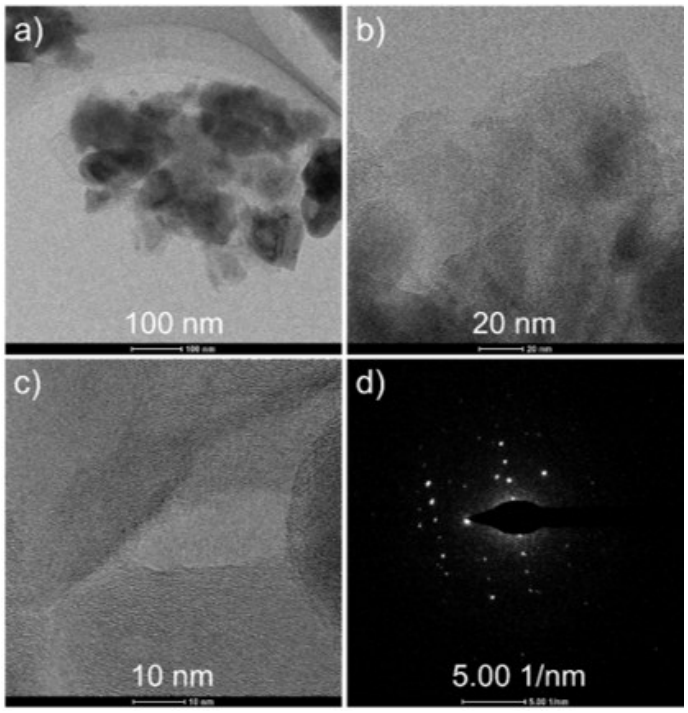

Figure 3. TEM Characterization of The PAN-PES Loaded Rgopks Sample. (a) Low Magnification TEM Image of the Sample. (b) HR-TEM Detail on the Geometrical Shape of the Flake Edges. (c) HR-TEM High Magnification Detail Showing a Number of Superimposed Rgopks Layers. (d) SAED Pattern Showing Diffuse Rings with Weak Diffraction Spots

The study by Dani et al. (2024) shows that the addition of activated carbon to EPS changes its color to gray due to the light-absorbing properties and deep black color of activated carbon. These findings indicate that the color changes occurring in the PAN-PES loaded rGOPKS solution are consistent with the optical characteristics of the filler material used. The darkening of the color in the PAN-PES loaded rGOPKS solution is mainly caused by the intrinsic properties of rGOPKS as a light-absorbing material. rGOPKS's intrinsic properties of rGO include a broad layered carbon-based structure with oxygen functional groups, such as hydroxyl, epoxide, and carbonyl groups. These functional groups facilitate strong interactions with the polymer matrix through hydrogen bonding (Gadtya et al., 2024). As the rGOPKS concentration increased from PPG10 to PPG20, the solution became progressively darker, indicating enhanced rGOPKS dispersibility. This observation aligns with our previous research on rGOPKS for supercapacitor applications, which also demonstrated a deepening black color with an increase in the rGOPKS content (Jauhari et al., 2021). The homogeneity of the solution is crucial for determining the quality of the resulting nanofibers. Figure 4b shows the nanofiber membranes derived from the pure PAN-PES solution (white) and PAN-PES solution with rGOPKS (PPG10-PPG20). In the subsequent stage, these solutions were transformed into nanofiber membranes using electrospinning. The results revealed a stark contrast between the membranes made from the pure PAN-PES solution and those containing rGOPKS (PPG10-PPG20). The pure membrane was white and smooth, whereas the rGOPKS-infused membrane exhibited a gray to black hue, indicating the successful integration of rGOPKS into the nanofibers. The incorporation of rGOPKS provides synergistic benefits, such as enhanced electrical conductivity and mechanical strength. The layered structure of rGOPKS also improves the mechanical and chemical interactions with the PAN-PES matrix through hydrogen bonding (Shahryari et al., 2021). Furthermore, rGOPKS's hydrophilic nature boosts the water absorption capacity of membranes, making them more suitable for filtration applications.

Figure 4c shows the longitudinal observation of the nanofiber membranes, comparing pure PAN-PES with PAN-PES loaded with rGOPKS. In the longitudinal orientation, the pure PAN-PES nanofiber membranes exhibited a smooth and uniform tubular structure. This morphology results from the electrospinning technique, which facilitates the formation of nanofibers with a controlled orientation along the longitudinal axis (Fitria et al., 2025). The incorporation of rGOPKS into the PAN-PES matrix significantly altered the longitudinal structure of the nanofibers. The PAN-PES membrane loaded with rGOPKS exhibited a rougher morphology and more complex surface texture. This is attributed to the distribution of rGOPKS within the polymer matrix, which creates micro- and nanoscale porous structures. These changes suggest that rGOPKS serves as a mechanical reinforcing material and influences the electrospinning process parameters, such as the flow rate and solution surface tension (Rinovian et al., 2025). Observation of the transverse position (Figure 4d) revealed the cross-sectional morphology of both pure PAN-PES nanofiber membranes and PAN-PES loaded rGOPKS composite membranes. The transverse cross-section of pure PAN-PES membranes displayed a uniform tubular structure. These nanofiber membranes could be bent to a radius of 1 cm, indicating excellent flexibility, as discussed in the mechanical analysis section. Consistent with these findings, previous research by Pervez et al. (2022) reported that electrospun membranes based on PAN and PES exhibited good mechanical stability without fracture, confirming the inherent elasticity of the polymer matrix. This structure reflects polymer compatibility, resulting in a well-distributed nanofiber matrix without significant deformation. In contrast, the PAN-PES loaded rGOPKS composite membrane exhibited a more complex transverse structure. The addition of rGOPKS resulted in nanofibers with smaller layered or hollow structures, as observed in the PPG10 to PPG20 membranes. The presence of rGOPKS also created a more intricate porous structure in the transverse cross-section, enhancing the filtration capacity and membrane permeability. These changes in the transverse morphology are crucial for determining the efficiency of membrane applications.

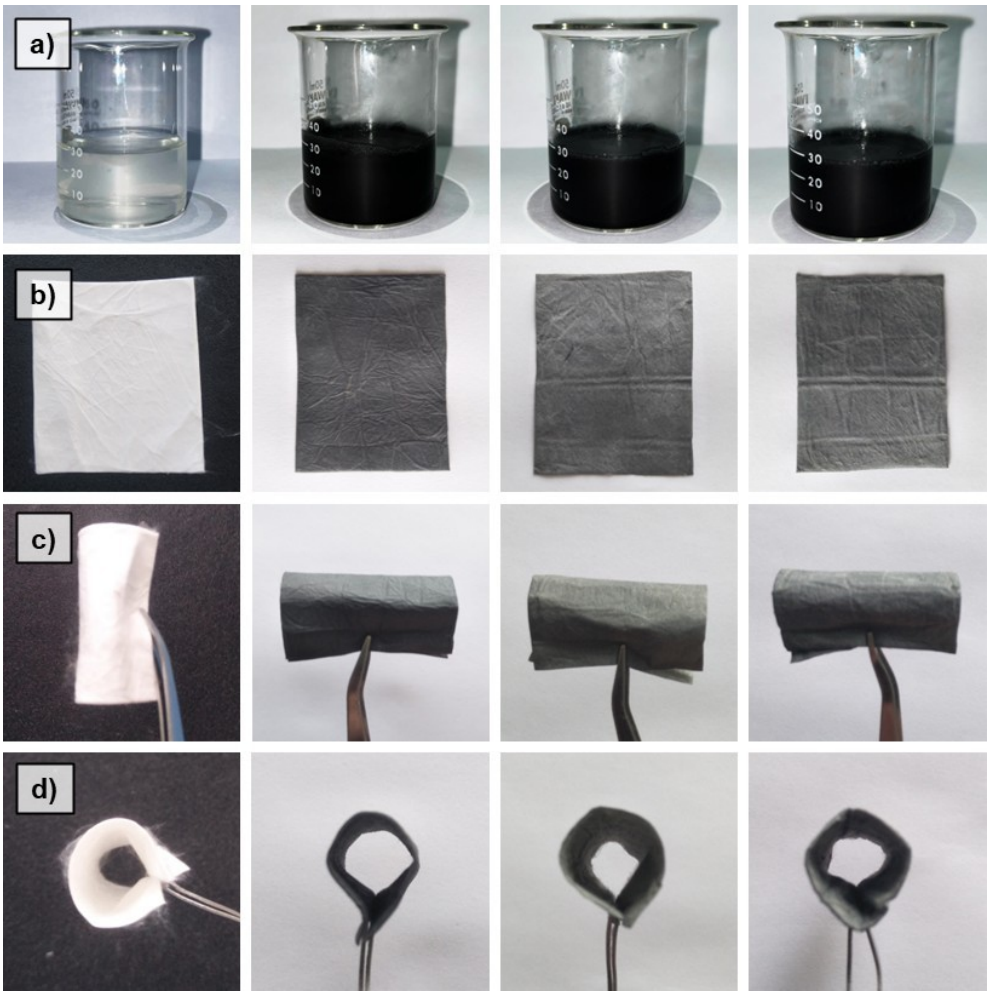

Figure 4. (a) PAN-PES Solution and PAN-PES Solution Loaded with rGOPKS (b) PAN-PES Nanofiber Membrane and PAN-PES Nanofiber Membrane Loaded with rGOPKS: PPG10, PPG15, and PPG20, in (c) Longitudinal Position and (d) Transversal Position

3.3 Morphology and Diameter of Nanofibrous Membrane

The surface morphology of nanofibers is a critical factor influencing their mechanical properties, porosity, and functional performance in filtration and separation applications. Figure 5 presents the SEM micrographs and corresponding fiber diameter distributions of electrospun PAN–PES loaded rGOPKS nanofiber membranes. The morphology and diameter distribution were analyzed using the Gaussian Amp (GaussAmp) model, which accurately represents a normal distribution with a symmetrical peak. The high correlation coefficients ($R^2 \geq 0.95$) confirmed the reliability of the fitting model for all samples (Almafie et al., 2022). In the PAN–PES Pure membrane (Figure 5a), the fibers exhibit a non-uniform morphology characterized by numerous bead formations, indicating instability during the electrospinning process. This phenomenon arises from the low viscosity and weak polymer chain entanglement in the 10 wt.% PAN–PES solution, which fails to sustain a stable jet under the influence of the electrostatic field (Denk et al., 2024). When viscosity is insufficient, the surface tension dominates the electrostatic force, leading to the breakup of the fluid jet into droplets that solidify as beads instead of forming continuous fibers. Furthermore, the absence of conductive fillers such as rGO results in low electrical conductivity, limiting charge accumulation on the jet and reducing stretching during flight. Consequently, bead fibers with poor uniformity were formed, with a mean diameter of 339.54 ± 95.40^{d} nm (R^2 = 0.95). Upon the incorporation of rGOPKS into the PAN–PES matrix at the same total polymer concentration (10 wt.%), the morphology improved significantly. The PPG10 nanofiber (Figure 5b) displayed smooth, uniform, and bead-free fibers with an average diameter of 389.22 ± 87.94^{c} nm (R^2 = 0.97). The elimination of beads is attributed to the enhanced electrical conductivity and increased charge density of the spinning solution induced by rGO nanosheets. The conductive rGO facilitates better jet elongation and reduces the Rayleigh instability that causes bead formation (Keshmiri et al., 2025). In

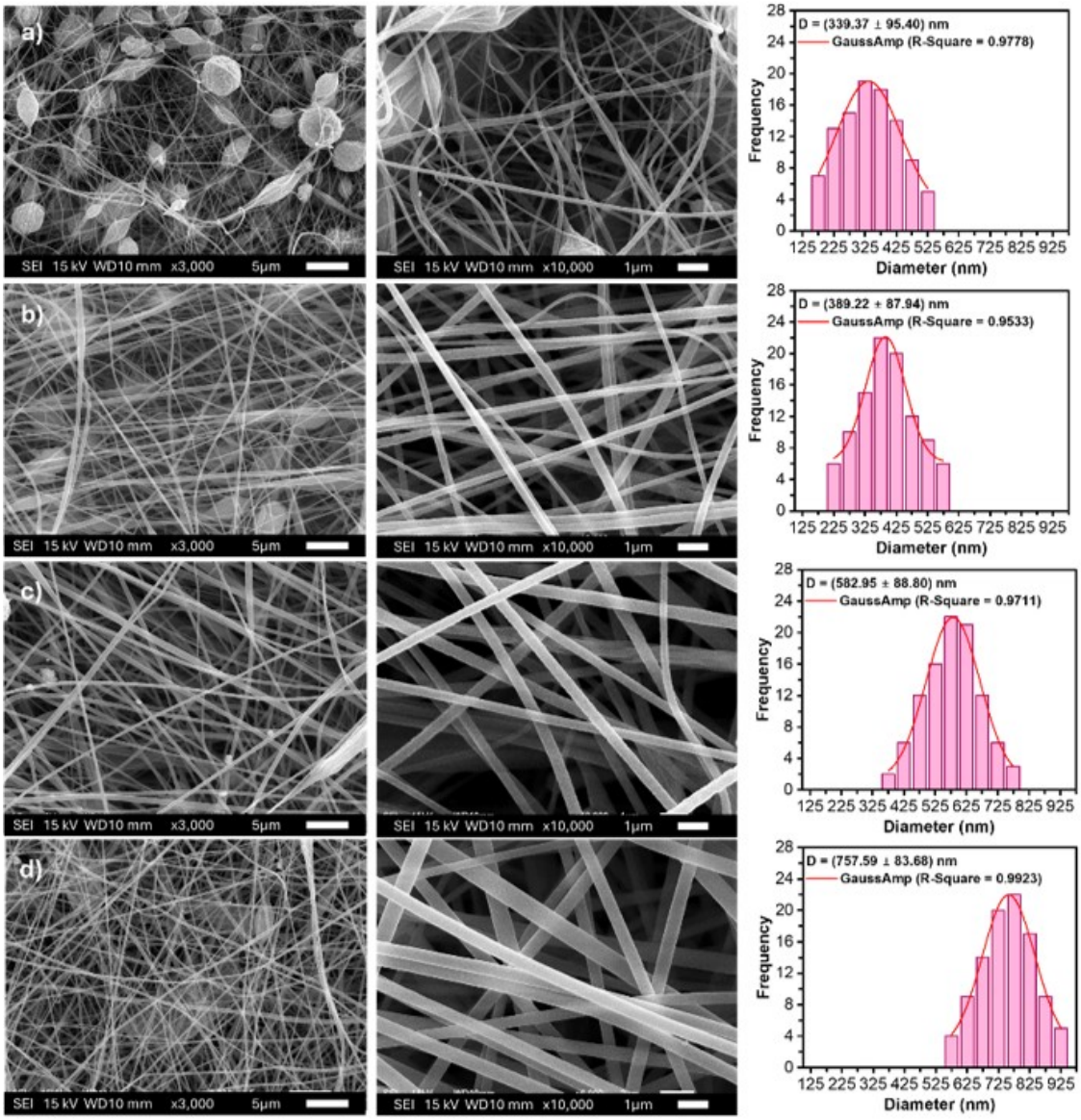

Figure 5. SEM Images and Diameter Distributions of the PAN-PES Loaded rGOPKS Nanofiber Membranes: (a) PAN-PES, (b) PPG10, (c) PPG15, and (d) PPG20

addition, rGOPKS enhances the intermolecular interaction and viscosity of the spinning solution through hydrogen bonding and $\pi-\pi$ stacking between rGOPKS and PAN-PES chains, improving jet stability during electrospinning. Similar findings were reported by Adabavazeh et al. (2025) who stated that the addition of conductive fillers can transform bead-containing fibers into uniform nanofibers due to improved electrostatic stretching forces.

As the polymer concentration increased to 15 wt.% (PPG15), the average fiber diameter rose to 582.95 ± 88.80b nm (R^2 = 0.96), with slightly reduced uniformity. The increased viscosity restricted jet stretching, leading to thicker fibers (Adabavazeh et al., 2025). A further increase to 20 wt.% (PPG20) resulted in the largest average diameter of 757.59 ± 83.68a nm (R^2 = 0.98), exhibiting a dense and interconne cted fiber network. The presence of different superscript capital letters among all samples confirms that the variations in average fiber diameter are statistically significant (p <0.05) based on the Two-way ANOVA and Tukey's post-hoc analysis (Qosim et al., 2025). The rise in fiber diameter with higher polymer concentration corresponds to stronger chain entanglement and reduced solvent evaporation, which limit the stretching of the polymer jet. In contrast, the PPG20 nanofiber, with a 20 wt.% concentration, displayed a larger and more uniform structure, featuring a more compact fiber arrangement and a larger average diameter of 757.59 nm with a standard deviation of 83.68 nm. Jang et al. (2020) suggested that Ag/rGO-PAN composite-modified membranes for water purification applications have an average

diameter of 544 ± 82 nm, maintaining a water flux of 658 L/m^2·h·bar. Li et al. (2020) found that super-hydrophilic electrospun PVDF/PVA mixed nanofiber membranes, with average diameters ranging from 1130 to 840 nm, can sustain maximum water fluxes of 1130 to 371 L/m^2·h·bar. Li et al. (2021) introduced a new PAN-ZnO electro-clean nanofiber membrane with superior water flux, having diameters between 200 and 400 nm, with the water flux of the nanofiber membrane gradually decreasing from 1140 L/m^2·h·bar to 959 L/m^2·h·bar as sputtering time increases. Thus, optimizing both polymer concentration and rGO loading is essential to produce defect-free, uniform PAN–PES loaded rGOPKS nanofiber membranes with excellent structural integrity for advanced water filtration applications.

3.4 FTIR Analysis

FTIR spectra were conducted to elucidate the chemical structure of the membrane. Figure 6 shows the FTIR spectra of the PAN–PES nanofiber membranes loaded with rGOPKS. The FTIR spectra in Figure 6 show the functional group characteristics of (a) rGOPKS, (b) PAN, and (c) PES. In the graphene spectrum (a), the weak absorption band around 3429 cm^{-1} indicates the O−H stretching of the hydroxyl group, while the bands at 2371 cm^{-1} and 1579 cm^{-1} are related to the aromatic C ≡ C and C=C vibrations, respectively, indicating a graphitic structure with little residual oxygenation. The PAN spectrum (b) shows a characteristic band at 2243 cm^{-1} which is the stretching absorption of the nitrile group (C ≡ N), while the bands at 2931 and 2870 cm^{-1} are from the aliphatic C−H stretching (Mokhtari-Shourijeh et al., 2020). The peaks around 1664, 1452, and 1357 cm^{-1} indicate the presence of C=O and C−H bending groups of the PAN polymer chain. Meanwhile, the PES (c) spectrum displays strong absorption bands at 1240–1105 cm^{-1} indicating asymmetric and symmetric stretching of sulfone groups (O=S=O), as well as bands at 1578 and 1488 cm^{-1} related to aromatic ring vibrations (Alsohaimi, 2024). The band at 3096 cm^{-1} indicates aromatic C−H stretching, while the absorption at 557 cm^{-1} confirms the C−O bond in the PES structure (Sam et al., 2021).

As depicted in this Figure 6, a broad peak at approximately 3440–3439 cm^{-1} signifies the stretching vibration of hydroxyl groups (-OH), which may stem from adsorbed water molecules or hydroxyl groups on the rGOPKS surface (Tohamy et al., 2024). This peak shifted slightly toward higher wavelengths as the polymer concentration increased, suggesting an enhanced capacity of the matrix to bind water owing to increased interactions between rGO and the polymer or an increase in the number of hydroxyl groups on the nanofiber surface. The peak at 2916–2800 cm^{-1} corresponds to the aliphatic C–H stretching vibration originating from the hydrocarbon structure in the PAN polymer molecules. This aliphatic C–H bond can be divided into five peaks, specifically those arising from asymmetric –CH_3 stretching (approximately 2922 cm^{-1}) and symmetric –CH_2 stretching (approximately 2850 cm^{-1}) (Yu et al., 2024). The characteristic nitrile (CN) peak at 2240–2241 cm^{-1} is linked to the C≡ N stretching vibration of the nitrile groups in PAN (Yu et al., 2024). This peak exhibited clear characteristics but was less intense than that of pure PAN, as previously reported (Sriyanti et al., 2024; Sriyanti et al., 2025). The presence of the nitrile group remained consistent, indicating that increasing the polymer concentration did not affect the fundamental structure of PAN. The polymer structure (aliphatic and nitrile bonds) remained stable during mixing with rGOPKS (Abdallah et al., 2023). No significant changes were observed in the intensity or position of these peaks among the three samples, suggesting that the basic structure of the polymer matrix was maintained even as the concentrations of PAN and PES increased.

The peak observed at approximately 1650 cm^{-1} corresponds to the stretching vibration of the carbonyl group (C=O) present in rGOPKS (Giraldo et al., 2025). This peak remained consistent, indicating that varying polymer concentrations did not influence the detectable amount of carbonyl groups. Furthermore, rGO was more uniformly distributed and interacted more effectively with the polymer. The G-band peak, located at approximately 1586 cm^{-1}, serves as a crucial marker of sp^2 groups associated with the C=C stretching vibration in highly ordered or more conjugated carbon structures (Sabet and Soleimani, 2022). This is reflected in the color of the nanofiber mat, which ranged from dark gray to black, depending on the layer thickness. The sp^2 group can engage in π-π interactions with aromatic groups or aliphatic chains in the polymer, thereby enhancing the homogeneity of the rGOPKS distribution within the polymer matrix and boosting the load-bearing capacity of the composite (Upadhyay et al., 2023). The sulfonate (-SO_2) region of PES, spanning 1400–1100 cm^{-1}, highlights a specific characteristic of PES. Two peaks, at approximately 1486 cm^{-1} and 1411 cm^{-1}, were identified as the stretching vibrations of the chemically stable integral benzene ring. Additionally, two peaks near 1298 cm^{-1} represent the asymmetric stretching vibration of the S=O bond, while the symmetric stretching vibration of this bond appears at 1148 cm^{-1} (Mokarami and Sereshti, 2024). Peaks below 1000 cm^{-1} indicate the deformation vibration of aliphatic C–H from PAN and C–O–C groups, resulting from changes in bond angles within the sulfone (-SO_2) structure and the benzene ring of PES (Ali et al., 2021). The FTIR spectrum revealed that the chemical structure of the rGOPKS-loaded PAN–PES nanofiber membrane remained stable, with a well-distributed array of functional groups and interactions that, in turn, supported enhanced structural stability, morphology, and mechanical properties, all of which are vital for applications such as water filtration.

3.5 XRD Analysis

X-ray diffraction (XRD) patterns, which are characteristic of each crystal phase, are well known to be influenced by the specific atomic arrangement within the crystal. The structural description of the synthesized membranes was examined using the powder X-ray diffraction model, as shown in Figure 7. The XRD profiles of all the membranes were similar, mak-

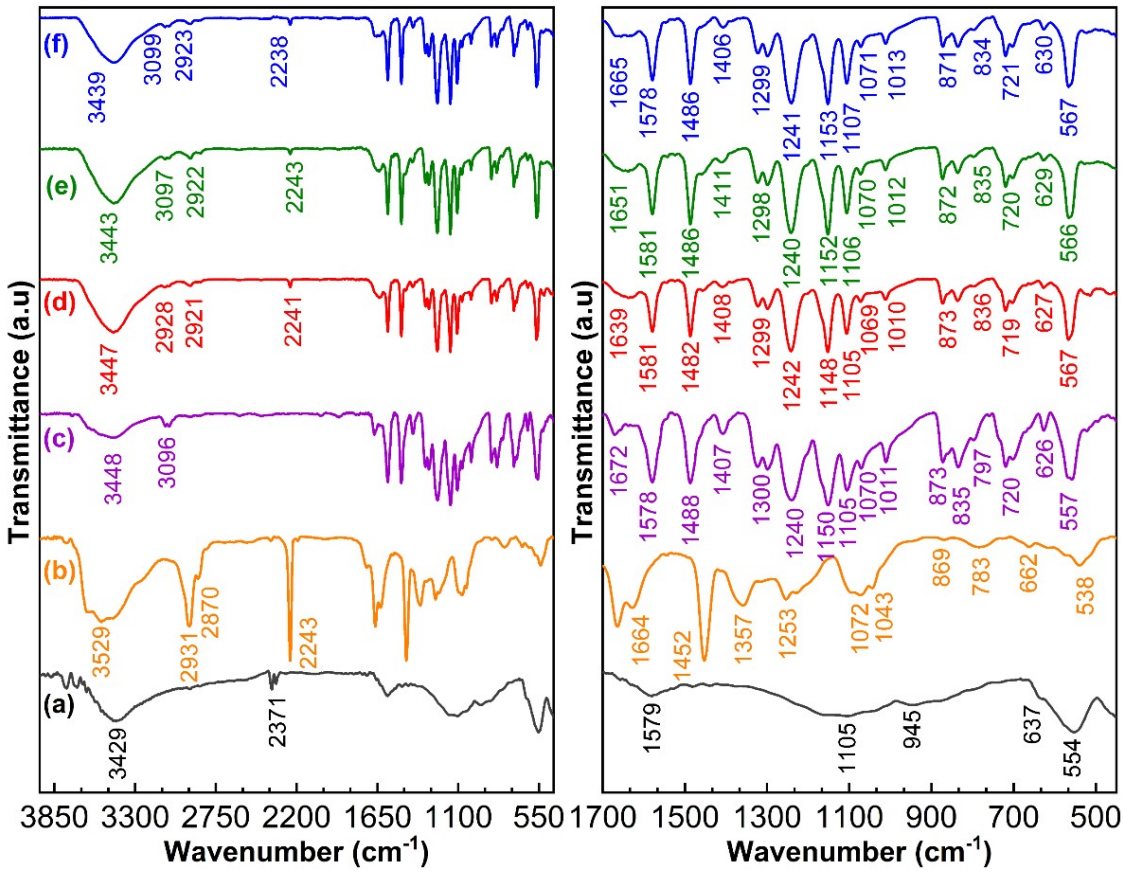

Figure 6. FTIR spectra of the (a) Graphene, (b) PAN, (c) PES, and PAN-PES Loaded rGOPKS Composite Nanofiber: (d) PPG10, (e) PPG15, and (f) PPG20

ing it difficult to identify significant changes. For all samples, broad peaks appeared in the range of 20–40°, which are characteristic of semicrystalline materials. The patterns of all three PAN-PES-loaded rGOPKS composite nanofibers exhibited dominant diffraction peaks at specific 2θ angles, associated with particular crystallographic planes. PPG10 has main peaks at 2θ = 17.79° (021), 21.23° (002), 23.61° (021), 26.45° (130), and 32.36° (131). PPG15 exhibited similar peaks but with slight shifts, such as at 2θ = 17.16° (021), 21.25° (002), 23.66° (021), 26.52° (130), and 32.46° (131). Meanwhile, PPG20 displays a pattern almost identical to that of PPG15, but with slightly higher intensity at certain peaks, such as at 2θ = 7.90° (021), 21.34° (002), 23.71° (021), and 32.49° (131). PES lacks a clear crystalline structure; therefore, it strongly depends on the degree of crystallinity and changes in the material structure. Pure PES typically exhibits relatively weak and broad peaks, with the main characteristic peak at approximately 2θ = 17.69°, reflecting its amorphous nature (Mohamat et al., 2022). PAN exhibited a diffraction pattern that reflected the properties of a semicrystalline polymer, with certain diffraction peaks indicating the formation of crystalline structures, although most of its structure was amorphous. PAN nanofiber membranes have a characteristic peak at approximately 2θ = 23.51° (Almafie et al., 2022). The characteristic peaks of rGOPKS indicate a distinct crystallographic structure that has been oxidized. Generally, rGOPKS exhibits a relatively sharp diffraction peak identifiable at 2θ = 21.23° (Jauhari et al., 2021). Additionally, a second peak appeared at 2θ = 32.36° due to the second carbon pairs found on adjacent chains (Vali et al., 2024). This peak is associated with the interplanar spacing (d-spacing), indicating the presence of oxygen layers on the graphene surface.

The XRD pattern revealed that rGOPKS served as a structural reinforcement within the PAN-PES matrix. XRD analysis also facilitates the calculation of crystal size using the Scherrer equation, providing insights into the dimensions of the crystalline domains in the material (Zhou et al., 2020). The distance between the crystallographic planes (d-spacing) is determined using Bragg's law, which correlates the position of the 2θ peak with the spacing between the crystal planes. In PPG10, the diffraction pattern indicates a relatively small crystal size (6.761 nm) and a large interplanar distance (7.4002 Å) (Ariyoshi et al., 2021). This suggests that, at lower PAN-PES concentrations (10 wt.%), the distribution of rGOPKS in the matrix is less uniform, resulting in a more random material structure. In contrast, PPG15, with a PAN-PES concentration of 15 wt.%, shows a more uniform distribution of

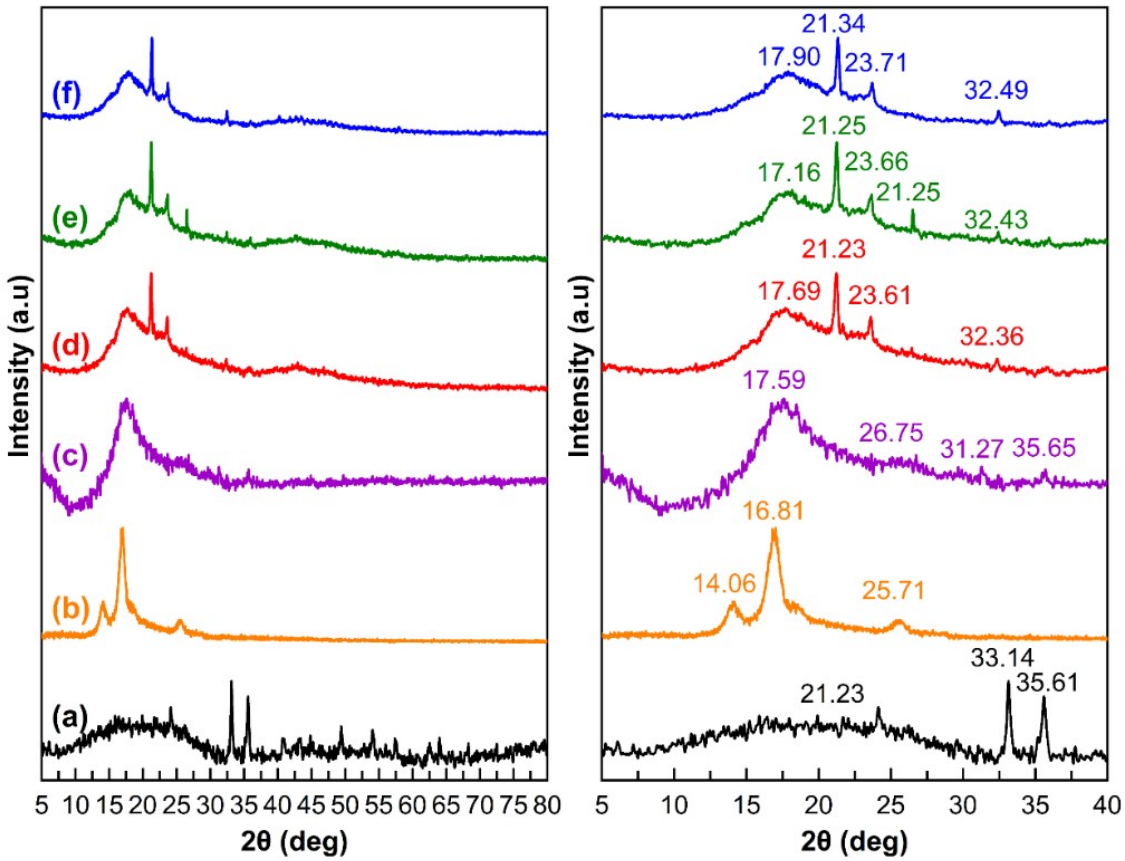

Figure 7. XRD Patterns Obtained from (a) Graphene, (b) PAN, (c) PES, and PAN-PES Loaded rGOPKS Composite Nanofibers: (a) PPG10, (b) PPG15, and (c) PPG20

rGOPKS, leading to a slightly larger crystal size (6.801 nm) and a more organized molecular structure. PPG20, with a PAN-PES content of 20 wt.% and a more concentrated distribution of rGOPKS, exhibits a sharper diffraction pattern, larger crystal size (6.901 nm), and a smaller d-spacing (4.159 Å). This indicates that the increased interaction between the polymer and rGOPKS contributed to a denser and more homogeneous structure (Hou et al., 2021). The improved rGOPKS distribution in PPG15 and PPG20 directly affected the nanofiber morphology. Nanofibers with more orderly semicrystalline structures tend to have smoother surfaces and more evenly distributed pores. These findings align with the measurements of the degree of crystallinity, which showed an increase in crystallinity with increasing PAN-PES concentration from PPG10 (24.63%) to PPG15 (31.53%) to PPG20 (33.52%). This reflects a greater molecular structural order in the material as the polymer concentration increases (Yang et al., 2020). The PAN-PES concentration was increased to 20 wt.% provides a sufficient number of polymer molecules to interact effectively, while optimal GO distribution acts as a nucleator that enhances the formation of crystalline domains. This high crystallinity imparts the strongest mechanical properties, enabling the material to withstand high mechanical pressure without significant deformation, thereby increasing its fouling resistance (El-Aswar et al., 2022). Additionally, the denser crystalline structure limits water absorption, further enhancing the material's resistance to fouling, which is particularly important in applications such as water filtration.

3.6 Mechanical Properties

Mechanical testing of electrospun nanofibers is the most direct method for examining their mechanical performance, as shown in Figure 8 and summarized in Table 2. We assessed the mechanical properties of the nanofibers through tensile testing using a universal testing machine (Almafie et al., 2022). The tensile behavior reflects the influence of intermolecular bonding, polymer homogeneity, and fiber morphology on mechanical integrity. Figure 8a displays the stress–strain curves, illustrating that increasing the PAN-PES concentration enhances the strength and elongation capability of the nanofiber mats. Figure 8b and Table 2 show that the strain at break increases significantly from 15.66 ± 0.75^{d}% (PAN-PES) to 22.09 $\pm$ 1.44^{c}% (PPG10), 35.36 ± 1.08^{b}% (PPG15), and 40.18 ± 2.21^{a}% (PPG20). The increase in strain corresponds to improved molecular flexibility and chain mobility due to better dispersion of rGOPKS and enhanced interfacial bonding between PAN, PES, and rGOPKS components (Upadhyay et al.,

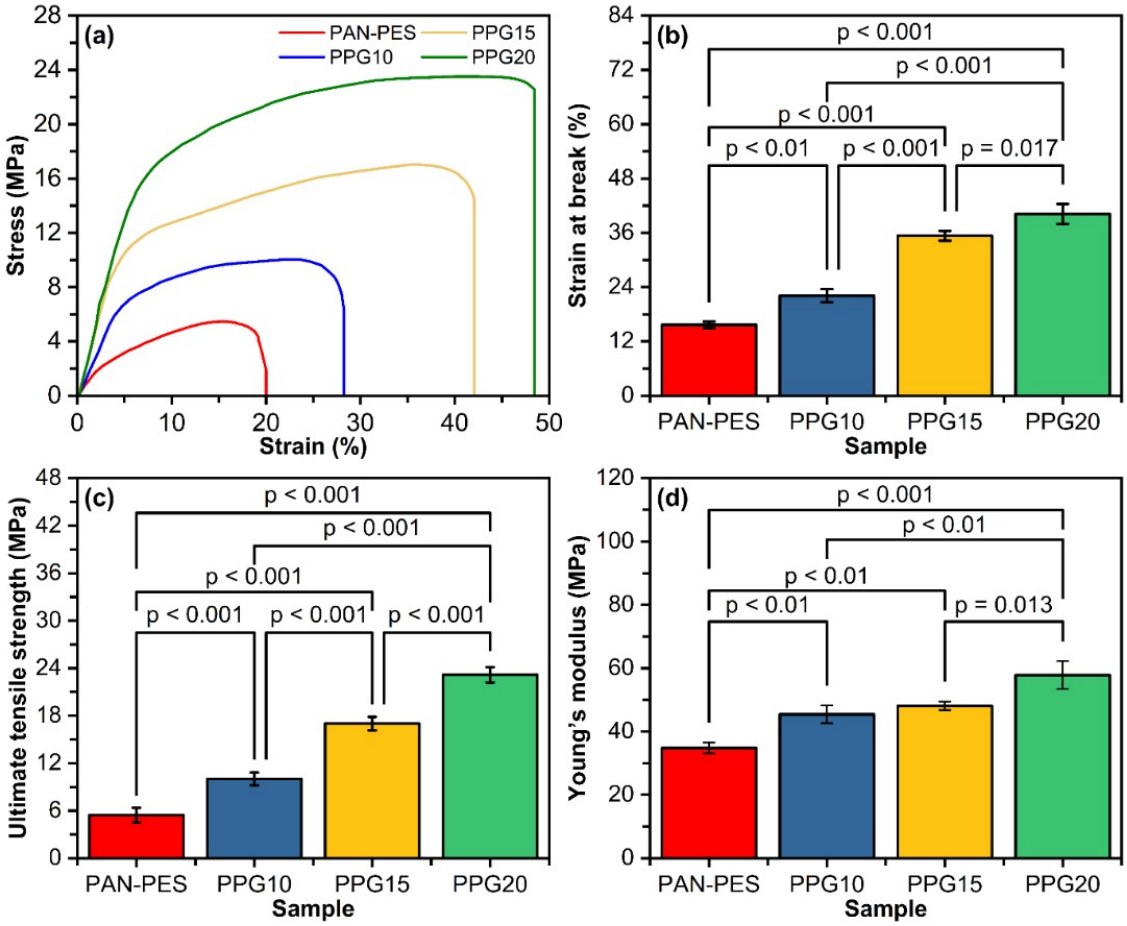

Figure 8. (a) Example of Tensile Stress–Strain Curves, (b) Strain at Break (%), (c) Ultimate Tensile Strength (MPa), and (d) Young's Modulus (MPa) for the PAN-PES Loaded rGOPKS Composite Nanofiber. Data are Expressed as Mean ± Standard Error (SE), (n = 3 for Each). One-Way ANOVA Followed by Tukey's HSD Multiple Pairwise Comparisons was Performed. Asterisks Indicate Statistically Significant Differences ($p < 0.05$)

Table 2. Mechanical Properties*

Sample	Strain at Break (%)	Ultimate Tensile Strength (MPa)	Young's Modulus (MPa)
PAN–PES	15.66 ± 0.75^{d}	34.79 ± 1.75^{d}	34.79 ± 1.76^{c}
PPG10	22.09 ± 1.44^{c}	45.43 ± 2.82^{c}	45.43 ± 2.82^{b}
PPG15	35.36 ± 1.08^{b}	48.11 ± 1.36^{b}	48.11 ± 1.36^{b}
PPG20	40.18 ± 2.21^{a}	57.83 ± 4.39^{a}	57.83 ± 4.39^{a}

**The values were expressed as the mean ± standard deviation of the three samples (n = 3). The use of superscripts in each column indicates a statistically significant difference between groups. In each column, values with different superscripts showed significant differences ($p < 0.05$).*

2023). The rise in elongation behavior can be attributed to the synergistic interactions among the functional groups of the polymers namely, the nitrile group (–C≡N) of PAN, the sp^2 carbon network of rGO (Yu et al., 2024), and the sulfon ($–SO_2$) group of PES which promote van der Waals, hydrogen bonding, and electrostatic interactions (Sarlak et al., 2012). These interactions improve compatibility and load transfer across the composite matrix, enhancing ductility and strength. Figure 8c and Table 2 further show the ultimate tensile strength, which increases progressively from 34.79 ± 1.75^{d} MPa (PAN-PES) to 45.43 ± 2.82^{c} MPa (PPG10), 48.11 ± 1.36^{b} MPa (PPG15), and 57.83 ± 4.39^{a} MPa (PPG20). The increase in tensile strength is attributed to better rGO dispersion and improved crystallinity within the PAN-PES network. Higher PAN-PES concentration enhances the formation of a dense polymer network, while rGO acts as a nanofiller, transferring stress effi-

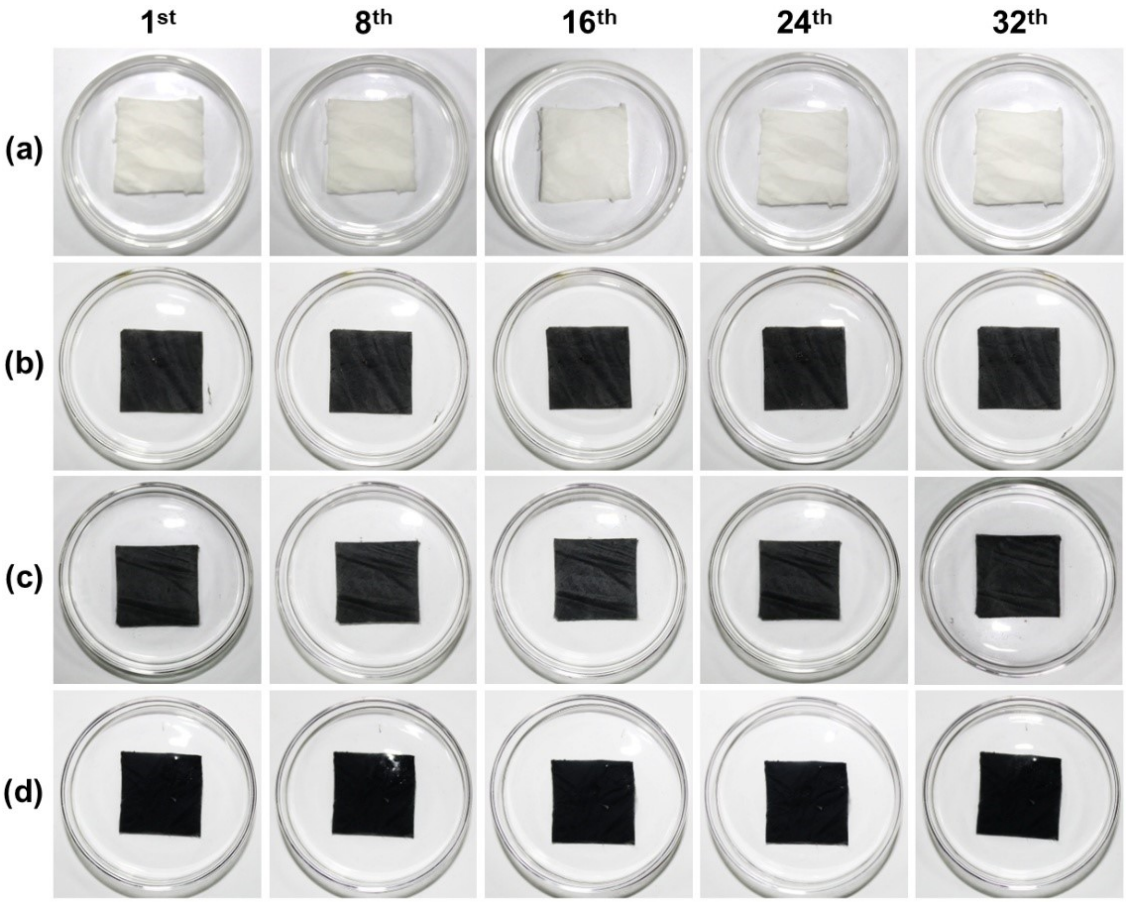

Figure 9. Thirty Two Days Water Resistance Test on PAN-PES Loaded rGOPKS Composite Nanofibers (a) PAN-PES Pure, (b) PPG10, (c) PPG15, and (d) PPG20

ciently across the fiber structure (Mohamat et al., 2022). The highest tensile strength in PPG20 is further supported by the increased crystallinity, as evidenced by the XRD analysis, which fortifies the internal structure of the material. This semicrystalline structure is crucial for strengthening the material, as the crystalline regions contribute to stiffness and strength, whereas the amorphous regions add elasticity (Jauhari et al., 2021). This phenomenon indicates a strengthened interfacial adhesion between the polymer chains and rGOPKS nanosheets, reducing void formation and mechanical failure. Prior research also supports these observations (Jauhari et al., 2021).

Figure 8d shows the Young's modulus values, which increase from 34.79 ± 1.76^{c} MPa (PAN-PES) to 45.43 ± 2.82^{b} MPa (PPG10), 48.11 ± 1.36^{b} MPa (PPG15), and 57.83 ± 4.39^{a} MPa (PPG20). The superscripts presented in each column represent statistically significant differences among the groups. Specifically, values within the same column that are labeled with different superscript letters indicate a significant difference between those groups ($p < 0.05$), while identical superscripts denote no significant variation. This upward trend demonstrates that higher PAN-PES concentrations lead to a more rigid and stable structure, as the molecular chains become more aligned and well-organized due to strong polymer-filler interactions (Yu et al., 2024). In water filtration applications, mechanical strength is a critical performance indicator, determining membrane lifetime and resistance to compaction. Chen et al. (2022) reported that the PAN/TPU composite exhibited a tensile strength of approximately 24.5 MPa and a Young's modulus of approximately 630.6 MPa. These properties enable the membrane to maintain flux stability. Leaper et al. (2021) also reported that the addition of functionalized graphene oxide (POSS-GO) to PVDF membranes increased tensile strength by up to 271% and elastic modulus by 38%, which contributed to enhanced mechanical stability and filtration performance. Thus, PPG20 nanofibers, with a tensile strength of 57.83 MPa and a Young's modulus of 57 MPa, have higher strength but lower stiffness compared to previous studies. This combination makes them ideal for water filtration membranes that are pressure-resistant and structurally stable. Therefore, the mechanical analysis confirms that increasing the PAN-PES concentration and incorporating rGOPKS substantially improve the nanofiber's tensile strength, elasticity, and stiffness. The statistically significant differences (denoted by different superscripts) validate the reliability of these im-

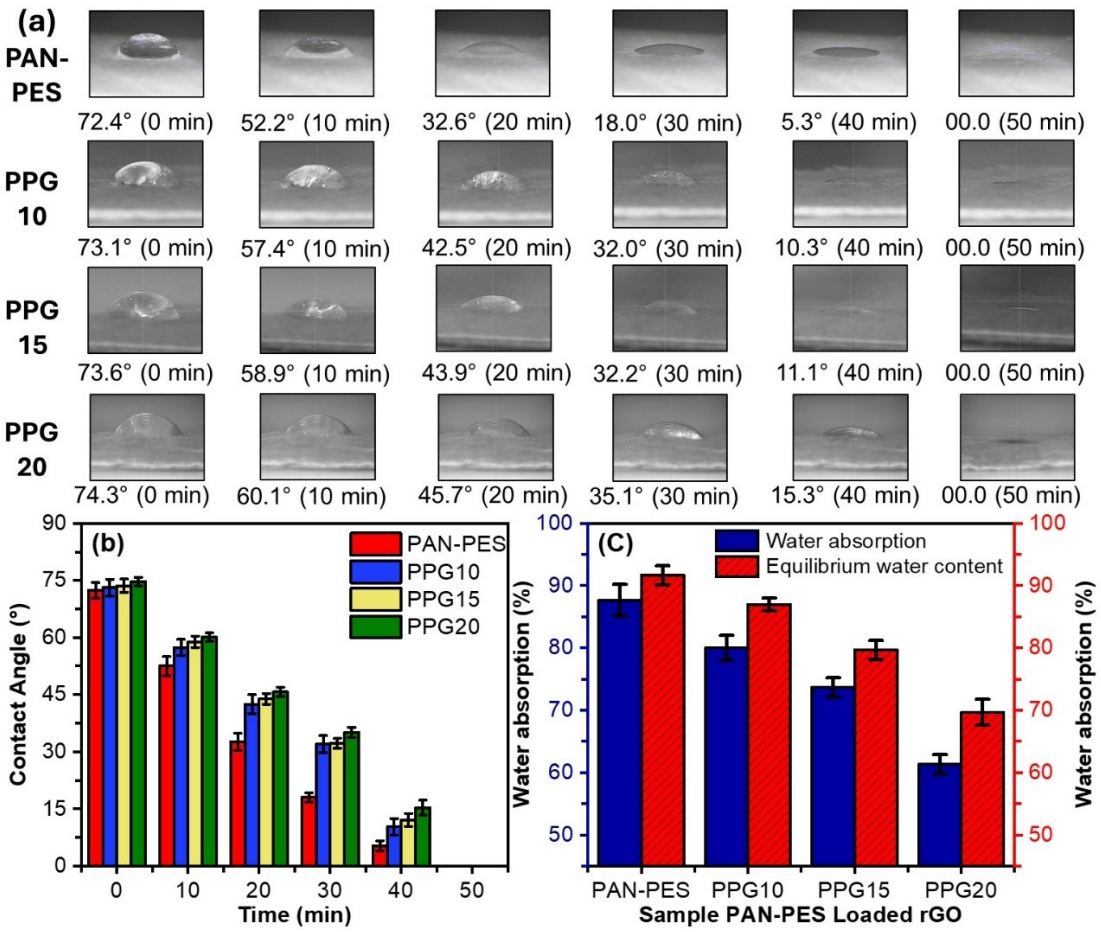

Figure 10. Wettability of Electrospun PAN-PES Loaded GO Composite Nanofibers. (a) Dynamic Water Contact Angle (WCA) Images, (b) Changing Curve of Dynamic WCA, and (c) Equilibrium Water Content and Water Absorption Rate

Table 3. Water Absorption and Equilibrium Water Content of PAN–PES and PAN–PES Loaded rGOPKS Composite Nanofiber Membranes*

Sample	Water Absorption (%)	Equilibrium Water Content (%)
PAN–PES	87.67 ± 2.52^{a}	91.67 ± 1.53^{a}
PPG10	80.00 ± 2.00^{b}	87.00 ± 1.00^{b}
PPG15	73.67 ± 1.53^{c}	79.67 ± 1.53^{c}
PPG20	61.33 ± 1.53^{d}	69.67 ± 2.08^{d}

**The values were expressed as the mean ± standard deviation of the three samples (n = 3). The use of superscripts in each column indicates a statistically significant difference between groups. In each column, values with different superscripts showed significant differences ($p < 0.05$).*

provements. These mechanical reinforcements are directly correlated with enhanced durability and stability during water filtration, positioning PPG20 as the optimal composition for high-performance membrane applications.

3.7 Water Resistance

Figure 9 presents the results of the 32-days water resistance test on rGOPKS-loaded PAN-PES composite nanofibers compared to pure PAN-PES. This test was designed to assess the structural stability of nanofibers under prolonged immersion, which is pertinent to water filtration applications. The samples tested included pure PAN-PES (a) and composites with rGOPKS at various PAN-PES concentrations: PPG10 (b), PPG15 (c), and PPG20 (d). For pure PAN-PES (a), the material's structure showed significant visual degradation by the 8th day, with discoloration and increasingly noticeable texture damage from the 16th to the 32nd day. This suggests that pure PAN-PES has low water resistance owing to weak intermolecular interactions within the polymer structure, making it susceptible to disintegration in aqueous environments (Mokarami and

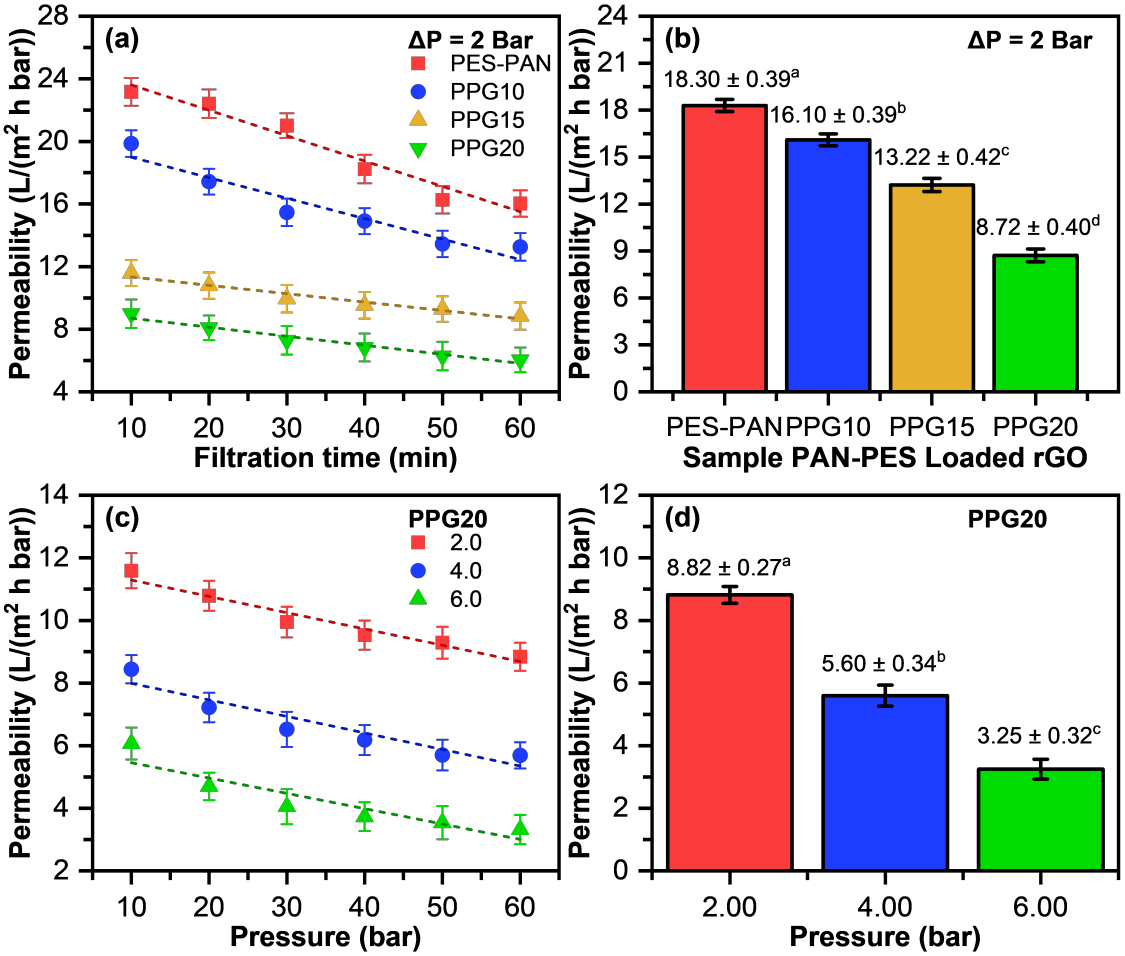

Figure 11. Filtration of Clean water as a Function of Each Membrane (a) Over Time and (b) The Final Values. Filtration of Clean Water as a Function of the Applied Pressure is Shown in (c) Over Time and (d) The Final Values. Values in each column are presented as mean ± SD, (i.e., n = 3). Means (± Standard Error) with Different Superscript in Each Column are Significantly Different at $p > 0.05$

Sereshti, 2024). In contrast, the composite nanofibers modified with rGOPKS demonstrated significantly better stability. PPG10 (b) maintained its form with slight changes from the 8th to the 16th day but began to show minor degradations after the 24th day. PPG15 (c) and PPG20 (d) exhibited superior water resistance compared to PPG10, with the material structure remaining intact without significant degradation up to the 32nd day.

Several previous studies have shown that morphological stability and water resistance are important factors in the performance of filtration membranes. Åkerlund et al. (2022) reported that PCL polymer experiences a very low mass loss (0.6%) after 4 weeks of immersion, indicating high stability against in-vitro degradation. Ebrahimi et al. (2022) found that electrospun PAN membranes with a GO/SiO_2 composite structure exhibited increased hydrophilicity and surface stability compared to pure PAN. While a study by Xue et al. (2020) reported that the graphene-oxide composite structure remained stable without significant morphological changes after being immersed for approximately 30 days. Based on the water resistance standards for filtration membranes (ASTM D570, ISO 62:2008, and JIS K7209), a material can be categorized as water-resistant if it is able to maintain at least 90% of its structural integrity and experiences a mass loss of less than 5% after 30 days of immersion.

Based on these standards and findings, the PAN-PES sample containing rGOPKS developed in this study meets the relevant water resistance criteria for water filtration applications. This is evidenced by the absence of visual degradation for up to 32 days and the ability to maintain fiber structure without loss of mechanical integrity. Functionally, the increased water resistance in PPG15 and PPG20 indicates that the addition of rGOPKS acts as a reinforcing agent that strengthens the bonds between polymer chains, reduces water absorption, and increases structural density. This effect enables the composite to have water resistance comparable to, or even exceeding,

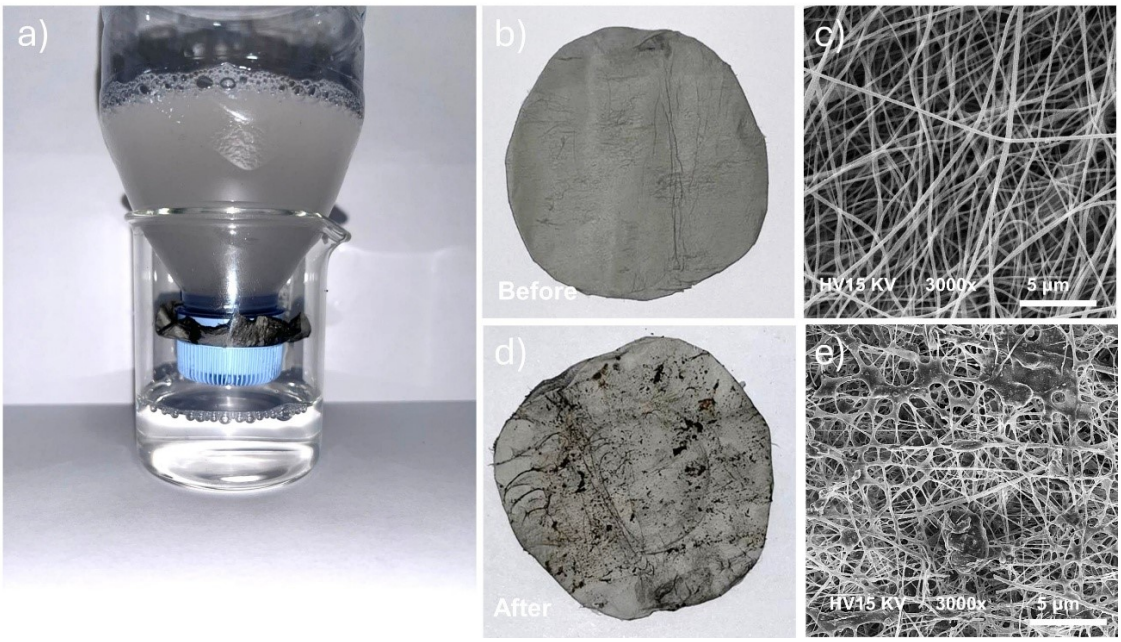

Figure 12. (a) Filtration Process using a Handmade Device Equipped with PAN/PES Nanofiber Membranes Containing rGOPKS, (b) Condition of the Filter Before Filtration, (c) Microscopic Appearance of Clean Nanofibers Without Contaminants, (d) Condition of the Filter After Filtration, and (e) Microscopic Appearance of Nanofibers with Residual Impurities

some commercial water filtration materials reported in previous studies. Thus, it can be concluded that PAN-PES loaded rGOPKS exhibits good water resistance characteristics and sufficient structural stability for long-term use in water filtration systems. PPG15 is considered the optimal formulation because it balances mechanical strength, structural density, and water resistance. While increasing the rGOPKS ratio up to PPG20 still demonstrates good performance, a slight decrease in elasticity indicates that too high a concentration can reduce membrane flexibility without significantly improving water resistance.

3.8 Water Contact Angle and Water Absorption Test

The phenomenon in which a liquid spreads on a solid surface is known as wetting behavior, and the contact angle measured using deionized water is termed the water contact angle (WCA) (Mousa et al., 2022). Figures 10a and 10b show the wettability of PAN-PES loaded rGOPKS nanofiber membranes with different rGOPKS contents, namely PPG10, PPG15, and PPG20. All samples initially exhibited hydrophobicity, with WCAs of about 73.1°-74.3°, but the angles gradually decreased to 0° within 50 minutes, indicating a transition toward hydrophilicity. This gradual reduction reflects a progressive wetting process, where water slowly infiltrates the porous nanofiber network. Such stable, sustained wetting is advantageous for filtration, as it prevents pore blockage, enhances permeability, and reduces fouling over time. The variation in WCA is influenced by fiber diameter and the presence of functional groups. SEM analysis showed that smaller nanofiber diameters provide a larger specific surface area, promoting stronger interactions between hydrophilic sites and water molecules (Dobosz et al., 2021). Among the samples, PPG10 had the smallest fiber diameter and thus the best hydrophilicity, while PPG20, with larger fibers, exhibited slower wetting behavior. This indicates that fiber morphology plays a key role in determining surface wettability. FTIR spectra confirmed the existence of hydrophilic functional groups such as hydroxyl (–OH) and carbonyl (–C=O), which enhance water affinity. Increasing rGOPKS content, particularly in PPG20, introduced more such groups, strengthening hydrogen bonding with water and improving overall wettability. Meanwhile, hydrophobic groups such as methyl and methylene ($–CH_3$) from the PAN-PES matrix slightly opposed wetting but had a lesser effect than the hydrophilic rGOPKS functionalities. Previous studies suggest that an optimal WCA for filtration membranes lies between 20°–60°, balancing hydrophilicity and structural stability. According to Liu et al. (2020), the addition of TiO_2 particles into the PAN matrix decreases the water contact angle to around 48.8°, thereby increasing the hydrophilicity and antifouling performance of the membrane (Liu et al., 2020). These studies collectively suggest that membranes with controlled and progressive reduction in contact angle, rather than immediate full wetting, maintain better structural endurance and filtration efficiency. Therefore, the PAN-PES loaded rGOPKS nanofibers developed in this study, particularly PPG10 and PPG15, meet the hydrophilicity criteria for efficient and durable water filtration membranes.

The equilibrium water content and water absorption rate of the PAN-PES loaded rGOPKS composite nanofiber membranes exhibited a gradual decrease with increasing PPG con-

Table 4. Previous Report for Water Filtration

Membrane Material	Diameter (nm)	Water Contact Angle	Water Flux ($L/m^2.h.bar$)	References
PVC@Ag/TiO_2	~ 370	–	~ 1300	(Zulfi et al., 2023)
TEOS/PSF	623 to 902	~ 67°	26.84 and 24.92	(Wu et al., 2024)
CNF/RSNF	128–106	~ 49° to ~ 85°	~ 27 to ~ 53	(Hassan et al., 2020)
Styrofoam/ACCS	590–610	126.5° and 131°	2162 to 8651 (1–4 bar from 15–60 s)	(Dani et al., 2024)
PAN–PES/rGO	389–757	72.4° to 74.3°	3.25 to 23 (2–6 bar from 1–60 min)	This study

centration, as shown in Figure 10c and Table 3. The equilibrium water content of the nanofiber membranes demonstrated a clear decreasing trend with increasing rGOPKS content. The pure PAN-PES membrane exhibited the highest value (91.67 ± 1.53[a]%), followed by PPG10 (87.00 ± 1.00[b]%), PPG15 (79.67 ± 1.53[c]%), and PPG20 (69.67 ± 2.08[d]%). This decline indicates that the incorporation of rGOPKS reduced the membrane's ability to retain moisture at equilibrium due to the partial hydrophobicity of rGOPKS and the decreased availability of hydrophilic functional groups. Similarly, the water absorption rate showed a progressive reduction from 87.67 ± 2.52[a]% for pure PAN-PES to 80.00 ± 2.00[b]% (PPG10), 73.67 ± 1.53[c]% (PPG15), and 61.33 ± 1.53[d]% (PPG20). Groups with the same superscripts within each column indicate that the values are not significantly different ($p > 0.05$). The lower absorption rate at higher rGOPKS content can be attributed to decreased porosity and increased compactness of the nanofiber network, which restrict water penetration into the membrane matrix. These results confirm that increasing PPG content enhances the hydrophobicity of the composite, leading to reduced water uptake. This finding corroborates the equilibrium water content trend, showing that PPG10 possesses a higher absorption capacity than PPG15 and PPG20. The results demonstrate a tunable wettability gradient from hydrophilic to hydrophobic surfaces by varying PPG concentrations. Such wettability control is often attributed to hierarchical micro-nano surface structures that modify surface energy (Liu et al., 2025). The results of this study are consistent with previous reports. For example, (Sun et al., 2021) reported that increasing the PVP fraction in PVP-PVDF nanofiber membranes significantly enhances water uptake capacity, reaching approximately 140-171% depending on polymer composition. Overall, these findings indicate that membranes with controlled and progressive wetting behavior exhibit superior structural durability and filtration efficiency. Therefore, the PAN-PES loaded rGOPKS nanofibers developed in this study, particularly PPG10 and PPG15, are suitable candidates for efficient and durable water filtration membranes.

3.9 Water Permeability

Water permeability (CWP) is a crucial parameter for evaluating membrane performance in filtration applications, as it reflects the membrane's ability to permit water flux under a specific transmembrane pressure without contamination. Quantitatively, CWP represents the membrane's capacity to allow water to pass through under a defined pressure gradient and serves as an indicator of both pore structure and surface hydrophilicity. As illustrated in Figure 11, CWP analysis was conducted on PAN–PES composite membranes with varying PPG and rGOPKS contents. In Figure 11a, the permeability of all membranes decreased linearly with increasing filtration time, indicating a time-dependent decline in water flux. This linear trend suggests that fouling and membrane compaction occur gradually rather than abruptly. At a constant pressure difference of $\Delta P = 2$ bar, the initial permeability of the pristine PAN–PES membrane was approximately 23 $L\,m^{-2}\,h^{-1}\,bar^{-1}$, whereas PPG10, PPG15, and PPG20 exhibited progressively lower initial permeabilities of about 20, 12, and 9 $L\,m^{-2}\,h^{-1}\,bar^{-1}$, respectively. Under the same operating pressure, the PPG10 membrane consistently showed higher permeability than PPG15 and PPG20. This behavior confirms that lower rGOPKS loading provides less resistance to water transport by maintaining a more open pore network. The gradual decline in permeability over time is attributed to progressive pore blockage and surface fouling caused by the adsorption of residual impurities or polymer chain rearrangement under hydraulic stress (Hami et al., 2023). In contrast, PPG20, which contains the highest rGOPKS concentration, exhibited the lowest permeability, decreasing from approximately 8 to 5 $L\,m^{-2}\,h^{-1}\,bar^{-1}$ within 60 min. This reduction is likely associated with rGOPKS aggregation within the polymer matrix, resulting in pore constriction or partial blockage. Moreover, increased rGOPKS content enhances membrane hydrophobicity, which further impedes water flux. In Figure 11b, a quantitative comparison shows that PAN–PES recorded a final permeability of 18.30 ± 0.39^{a} $L\,m^{-2}\,h^{-1}\,bar^{-1}$, followed by PPG10 ($16.10\pm0.39^{b}$), PPG15 ($13.22\pm0.42^{c}$), and PPG20 ($8.72 \pm 0.40^{d}$). The different superscripts indicate statistically significant differences among the samples ($p < 0.05$), confirming that rGOPKS loading has a pronounced effect on membrane permeability. The substantial reduction from PAN-PES to PPG20 suggests that excessive rGOPKS content decreases water flux due to combined pore constriction and interfacial incompatibility between rGOPKS sheets and the polymer matrix.

Figure 11c further examines the pressure-dependent performance of the PPG20 membrane. Permeability decreased linearly with increasing operating pressure and filtration time, indicating that membrane compaction becomes more severe at elevated pressures. This structural densification reduces effective pore size and limits water transport (Mohamat et al., 2022). As shown in Figure 11d, the final permeability decreased from 8.82 ± 0.27^{a} L m^{-2} h^{-1} bar^{-1} at 2 bar to 5.60 ± 0.34^{b} at 4 bar and 3.25 ± 0.32^{c} at 6 bar. This inverse relationship between pressure and permeability demonstrates that, beyond 4 bar, mechanical compaction dominates over the increased driving force, resulting in lower net flux. Therefore, operation at moderate pressure (approximately 2 bar) provides an optimal balance between driving force and structural integrity. Previous studies have reported significantly higher permeability values through surface modification strategies. For instance, (Ibrahim and Hilal, 2023) demonstrated that diamond and honeycomb surface patterning on PES-based ultrafiltration membranes increased clean water permeability to approximately 76.6 ± 16.9 L m^{-2} h^{-1} bar^{-1}. Similarly, Zhao et al. (2021) reported that feed-spacer-inspired surface patterning enhanced membrane permeance to 110 ± 17 L m^{-2} h^{-1} bar^{-1} under optimal conditions. Compared with these reports, the permeability of PPG20 (8.82–3.25 L m^{-2} h^{-1} bar^{-1}) is lower; however, this is reasonable considering the high rGOPKS loading, which inherently increases flow resistance. The relatively low permeability observed in this study is primarily attributed to membrane densification, increased nanofiber diameter due to high rGOPKS content, and the absence of surface patterning strategies commonly employed in high-flux membranes. These findings demonstrate that both rGOPKS loading and operating pressure strongly influence CWP behavior. Lower additive concentration and moderate pressure preserve membrane porosity, whereas excessive rGOPKS loading or high operating pressure accelerates compaction and flux decline. Maintaining permeability above 8 L m^{-2} h^{-1} bar^{-1} is therefore desirable for sustainable clean water filtration. Overall, the water permeability behavior observed in this study is governed by membrane compaction under pressure, nanofiber diameters in the range of 389–757 nm, moderate hydrophilicity (water contact angle 72.4 – 74.3°), and continuous filtration at 2–6 bar for 60 min (Firdaus et al., 2025b; Firdaus et al., 2025a). This behavior is consistent with the findings of Wu et al. (2024), who reported a comparable permeability of 24.92 L m^{-2} h^{-1} bar^{-1} for membranes with similar fiber diameters and contact angles, confirming that the permeability values obtained in this study are structurally reasonable.

3.10 Surface Morphological of Nanofiber Before and After Wastewater Filtration

Figure 12 shows the water filtration process using a simple device equipped with a PAN-PES nanofiber membrane containing rGOPKS. Figure 12(a) illustrates the filtration of river water, which appears cloudy due to the presence of suspended particles, fine silt, and dissolved organic materials. This condition is a common characteristic of surface water, especially in river basins that receive runoff from domestic and agricultural activities. The high level of turbidity indicates the presence of total suspended solids (TSS) and organic compounds such as humic substances and tannins, which can cause clogging (fouling) in the membrane pores during the filtration process (Certiat et al., 2024). Before the filtration process, as shown in Figure 12(b), the membrane surface appears clean, with a homogeneous color, and shows no signs of contamination. Meanwhile, microscopic observations in Figure 12(c) reveal a smooth, uniform, and interconnected nanofiber network structure, with fiber diameters in the micrometer range. This morphology indicates an optimal electrospinning result, where the even distribution of fibers and high porosity allow water to flow smoothly through the gaps between the fibers while providing a large surface area for capturing fine particles. These structural characteristics are consistent with the findings of Zeng et al. (2023), who reported that a layer of chitosan nanofibers produced by electrospinning with a pore size of approximately 274 nm and a thickness of ±10 μm was capable of generating a very high water flux of up to 107.53 L.m^{-2}.h^{-1} in forward osmosis applications. This demonstrates that a porous and uniform nanofiber structure significantly enhances water permeability and reduces the tendency for membrane fouling.

After the filtration process, the membrane surface condition changed significantly as shown in Figure 12(d). The membrane color became darker due to the accumulation of particles and the deposition of contaminants on its surface. This color change is an indication of fouling, which is blockage caused by solid particles and organic materials adhering to the fibers. Figure 12(e) shows the nanofiber surface after filtration, where the fiber network appears to be covered by an irregular layer of residue, indicating the adsorption of particles onto the fiber surface. These findings indicate that the filtration mechanism relies not only on the physical screening process but also involves active chemical interactions between the functional groups of rGOPKS and the contaminant molecules or ions in the water (Dani et al., 2024). These results are consistent with another research report by Elessawy et al. (2024) which also stated that the addition of graphene oxide (GO) to the PES nanofiber matrix enhances the adsorption capacity for organic compounds and heavy metals, thanks to the presence of active oxygen groups on its surface. Morphological changes before and after filtration demonstrate the effectiveness of the PAN-PES membrane loaded with rGOPKS in capturing solid contaminants from river water. The dense fiber structure and even distribution of rGO help enhance the membrane's filtration capacity and resistance to fouling. These results indicate that rGO-polymer composite nanofiber technology has great potential to be applied as a simple yet efficient water filtration system in areas with poor surface water quality. Previous reports on nanofibrous membranes for water filtration are summarized in Table 4.

4. CONCLUSIONS

Empirical evidence suggests that the concentration of the PAN-PES core solution significantly influences the fiber diameter, mechanical properties, water contact angle, water absorption, water resistance, and clean water permeability. PPG10-PPG20 samples, defect-free, bead-free, and geometrically uniform nanofiber membranes were produced, with nanofiber pore channel diameters ranging from 389 to 757 nm. The nanoscale fiber diameter of PAN-PES loaded with rGO provides a substantial surface area, enhancing the absorption capacity and membrane separation performance. Characterization revealed that the formation of hydrogen bonds between PAN-PES loaded with rGO effectively enhanced the hydrophilicity of the membrane. Distinct crystallization peaks were observed, with a maximum crystallinity of 33.52%. The modulus increased markedly from 34.79 to approximately 57.83 MPa as the fiber diameter increased. The dependence of the modulus on the diameter suggests that the fiber cross-section is homogeneous. A rough nanostructure was formed on the membrane surface following the incorporation of rGO particles onto the PAN surface, significantly increasing the hydrophobicity of the membrane (WCA 74.3°) with an equilibrium water content of 91%. The nanofiber membranes exhibited resistance to immersion for 32 d. PPG10 maintained a strong permeability (16.10 L/m^2.h.bar), PPG15 maintained a stable permeability (13.22 L/m^2.h.bar), and PPG20 maintained a weak permeability (8.72 L/m^2.h.bar). This study demonstrates that the resulting electrospun membrane successfully enhanced the surface properties and improved the filtration performance with high flux. Furthermore, morphological analysis shows that the PAN-PES membrane loaded with rGO is effective in capturing suspended solids and preventing fouling, confirming its potential as an efficient medium for sustainable water purification.

5. ACKNOWLEDGMENT

The research/publication of this article was funded Universitas Sriwijaya 2025. In accordance with the Rector's Decree Number: 0029/UN9/LPPM.PT/2025, on September 17, 2025.

REFERENCES

Ab Aziz, N. A. H., U. F. Md Ali, A. A. Ahmad, M. I. H. Mohamed Dzahir, M. H. Khamidun, and M. F. Abdullah (2023). Non-Functionalized Oil Palm Waste-Derived Reduced Graphene Oxide for Methylene Blue Removal: Isotherm, Kinetics, Thermodynamics, and Mass Transfer Mechanism. *Arabian Journal of Chemistry*, **16**(1)

Abdallah, F., E. K. Arthur, K. Mensah-Darkwa, E. Gikunoo, S. A. Baffour, B. A. Agamah, and F. O. Agyemang (2023). Electrochemical Performance of Corncob-Derived Activated Carbon–Graphene Oxide and TiO_2 Ternary Composite Electrode for Supercapacitor Applications. *Journal of Energy Storage*, **68**

Adabavazeh, Z., N. Johari, and F. Baino (2025). Electrospun Conductive Polymer Scaffolds: Tailoring Fiber Diameter and Electrical Properties for Tissue Engineering Applications. *Materials Today Communications*, **46**; 112596

Adhikary, K. and P. Goswami (2025). Synthesis of Eco-Friendly rGO/ZrP Nanocomposite as Novel Adsorbents for Enhanced Non-Enzymatic Salicylic Acid Delivery. *Next Nanotechnology*, **7**; 100142

Åkerlund, E., A. Diez-Escudero, A. Grzeszczak, and C. Persson (2022). The Effect of PCL Addition on 3D-Printable PLA/HA Composite Filaments for the Treatment of Bone Defects. *Polymers*, **14**(16)

Ali, A. B., D. Slawig, A. Schlosser, J. Koch, N. C. Bigall, F. Renz, and R. Sindelar (2021). Polyacrylonitrile (PAN) Based Electrospun Carbon Nanofibers (ECNFs): Probing the Synergistic Effects of Creep Assisted Stabilization and CNTs Addition on Graphitization and Low Dimensional Electrical Transport. *Carbon*, **172**

Alimohammady, M., M. Jahangiri, M. Salavati-Niasari, and A. M. Aljeboree (2025). Heavy Metal Adsorption by Graphene Oxide Modified with 5-Amino-3(2-Thienyl)Pyrazole Using Central Composite Design/Response Surface Methodology (CCD/RSM). *RSC Advances*, **15**(44); 36837–36860

Almafie, M. R., A. Fudholi, R. Dani, M. K. N. A. Idjan, I. Royani, and I. Sriyanti (2025). Effects of Electrospinning Parameters on Polycaprolactone Membrane Diameter: An Investigation Utilizing Central Composite Design and Characterization. *Results in Engineering*, **25**; 104002

Almafie, M. R., L. Marlina, R. Riyanto, J. Jauhari, Z. Nawawi, and I. Sriyanti (2022). Dielectric Properties and Flexibility of Polyacrylonitrile/Graphene Oxide Composite Nanofibers. *ACS Omega*, **7**(37); 33087–33096

Alsohaimi, I. H. (2024). Comparative Study of PS and PES and Their Sulfonated Forms in Antifouling Behavior and Rejection Efficiency. *Journal of King Saud University - Science*, **36**(11); 103576

Ariyoshi, S., S. Hashimoto, S. Ohnishi, S. Negishi, H. Mikami, K. Hayashi, and N. Hiroshiba (2021). Broadband Terahertz Spectroscopy of Cellulose Nanofiber-Reinforced Polypropylenes. *Materials Science and Engineering: B*, **265**; 115000

Askari, A., S. R. Nabavi, and A. Omrani (2024). Fabrication of PES/PAN Electrospun Nanofiber Membrane Incorporated with [EMIM][Ac] Ionic Liquid for Oil/Water Separation. *Journal of Water Process Engineering*, **65**; 105768

Certiat, M., J. Teychené, C. Guigui, S. Laborie, and F. Jolibois (2024). Tannic Acid Self-Aggregation and Adsorption onto a Polyethersulfone Membrane: An All-Atom Molecular Dynamics Study. *Journal of Membrane Science*, **697**; 122570

Chen, Y., N. Wang, M. Jensen, and X. Li (2022). Low-Temperature Welded PAN/TPU Composite Nanofiber Membranes for Water Filtration. *Journal of Water Process Engineering*, **47**; 102806

Dani, R., Ismet, L. Marlina, R. Alisya, M. A. K. Aldi, A. Ludian-Syah, and I. Sriyanti (2024). Synthesis of Activated Carbon from Coconut Shell and Recycled Styrofoam Nanofiber for Water Filtration. *Makara Journal of Science*, **28**(4); 357–369

Davidová, M., J. Tokarský, L. Kulhánková, S. Vallová, L. Řeháčková, M. Ritz, and M. Kormunda (2024). Graphite and Multi-Layer Graphene from a Low Molecular Weight Carbon Source. *Carbon*, **230**; 119662

Denk, J., X. Liao, W. Knolle, A. Kahnt, A. Greiner, S. Schafföner, and G. Motz (2024). Novel Multifibrillar Carbon and Oxidation-Stable Carbon/Ceramic Hybrid Fibers Consisting of Thousands of Individual Nanofibers with High Tensile Strength. *Scientific Reports*, **14**(1); 18143

Dobosz, K. M., C. A. Kuo-Leblanc, J. W. Bowden, and J. D. Schiffman (2021). Robust, Small Diameter Hydrophilic Nanofibers Improve the Flux of Ultrafiltration Membranes. *Industrial and Engineering Chemistry Research*, **60**(25); 9179–9188

Ebrahimi, F., S. R. Nabavi, and A. Omrani (2022). Fabrication of Hydrophilic Special Sandwich Structure of PAN/GO/-SiO_2 Electrospun Membrane Decorated with SiO_2 Nanoparticles for Oil/Water Separation. *Journal of Water Process Engineering*, **48**; 102926

Edokali, M., M. Mehrabi, O. Cespedes, C. Sun, S. M. Collins, D. Harbottle, and A. Hassanpour (2024). Antifouling and Stability Enhancement of Electrochemically Modified Reduced Graphene Oxide Membranes for Water Desalination by Forward Osmosis. *Journal of Water Process Engineering*, **59**; 104809

El-Aswar, E. I., H. Ramadan, H. Elkik, and A. G. Taha (2022). A Comprehensive Review on Preparation, Functionalization and Recent Applications of Nanofiber Membranes in Wastewater Treatment. *Journal of Environmental Management*, **301**; 113908

Elessawy, N. A., J. Exley, D. S. El-Sayed, A. Toghan, S. A. Al-Hussain, M. Elzokm, and M. Tillotson (2024). Development of an Efficient, Low-Operating-Pressure Graphene Oxide/Polyethersulfone Nanofiltration Membrane for Removing Various Water Contaminants. *Journal of Environmental Chemical Engineering*, **12**(2); 112489

Faaizatunnisa, N., R. Ediati, E. N. M. D. Yusof, A. Fadlan, K. Karelius, U. Kulsum, and M. N. Ariesta (2025). Optimized Photocatalytic Degradation of 2-Naphthol Using ZnO/rGO Nanocomposites Synthesized from Palm Kernel Shell Waste. *Journal of Water Process Engineering*, **70**; 106977

Firdaus, A., R. Dani, M. S. P. Gantada, A. F. Ismail, N. Nukman, I. Bizzy, and A. Mataram (2025a). Identifying the Features of Mechanical and Physicochemical Characteristics of Polyethersulfone Membranes Using Electric Field Method for Water Filtration Applications. *Eastern-European Journal of Enterprise Technologies*, **6**(6); 14–27

Firdaus, A., S. Nasir, R. Dani, I. N. Prasatya, A. F. Ismail, M. H. D. Othman, and A. Mataram (2025b). Synthesis of Polyethersulfone Membranes with the Addition of Silver Nitrate for Water Filter Applications. *EUREKA: Physics and Engineering*, **2025**(1); 121–131

Fitria, S., M. R. Almafie, I. Alfikro, F. Monado, I. Sriyanti, and I. Royani (2025). Synthesis and Characterization of Polyvinyl Alcohol (PVA) Nanofiber Membranes with Annona muricata and Terminalia catappa Leaf Extract. *Science and Technology Indonesia*, **10**(3); 857–866

Gadtya, A. S., D. Tripathy, L. Rout, and S. Moharana (2024). Graphene Oxide, Its Surface Functionalisation, Preparation and Properties of Polymer-Based Composites: A Review. *Composite Interfaces*, **31**

Giraldo, L., C. A. G. Fajardo, and J. C. M. Piraján (2025). Innovative Chitosan/Graphene Oxide Composites: A Thermodynamic and Calorimetric Approach to Pharmaceutical Waste Removal from Water. *Results in Engineering*, **25**; 103697

Hami, S. S. B. M., N. D. N. Affandi, L. Indrie, S. Tripa, A. M. Harun, and M. R. Ahmad (2023). Enhancing Mechanical Properties and Flux of Nanofibre Membranes for Water Filtration. *Polymers*, **15**

Hassan, M. L., S. M. Fadel, R. E. Abouzeid, W. S. Abou Elseoud, E. A. Hassan, L. Berglund, and K. Oksman (2020). Water Purification Ultrafiltration Membranes Using Nanofibers from Unbleached and Bleached Rice Straw. *Scientific Reports*, **10**(1)

Hou, C., M. A. A. Newton, B. Xin, and T. Li (2023). Preparation and Characterization of Unidirectional Water-Transported Bilayer PLA/ZnO-PAN/SPA Nanofibrous Membrane for Wound Healing. *Colloids and Surfaces A: Physicochemical and Engineering Aspects*, **676**; 132308

Hou, J., J. Yun, W. Jang, J. H. Kim, and H. Byun (2021). Polyacrylonitrile Nanofiber Membranes Incorporated with Large Reduced Graphene Oxide Content In Situ. *Journal of Materials Science*, **56**(33)

Ibrahim, Y. and N. Hilal (2023). Enhancing Ultrafiltration Membrane Permeability and Antifouling Performance through Surface Patterning with Features Resembling Feed Spacers. *NPJ Clean Water*, **6**(1)

Idjan, M. K. N. A., Fatmawati, M. R. Almafie, R. Dani, Subandrate, A. Fudholi, and I. Sriyanti (2025). Physicochemical Properties and Antioxidant Activity of PVP/CA Membranes Nanofiber Loaded Arcangelisia flava L. Merr. Stem Extract Using Electrospinning Technique. *Next Materials*, **8**; 100839

Jang, W., J. Yun, Y. Park, I. K. Park, H. Byun, and C. H. Lee (2020). Polyacrylonitrile Nanofiber Membrane Modified with Ag/GO Composite for Water Purification System. *Polymers*, **12**(11); 2441

Jauhari, J., M. R. Almafie, L. Marlina, Z. Nawawi, and I. Sriyanti (2021). Physicochemical Properties and Performance of Graphene Oxide/Polyacrylonitrile Composite Fibers as Supercapacitor Electrode Materials. *RSC Advances*, **11**(19); 11233–11243

Joshi, R., M. P. Narayanaswamy, S. Sinha, A. Dey, G. Rastogi, D. Rangappa, and I. Lahiri (2024). Reduced-Graphene-Oxide-Based Thin Films: An Alternative Coating for Harsh Space Environments. *ACS Applied Materials & Interfaces*, **16**(50); 69690–69702

Keshmiri, N., P. Najmi, A. S. Milani, and M. Arjmand (2025). Electrospinning for Electromagnetic Interference Shielding: Principles, Challenges, and Future Directions. *Carbon*, **245**;

120831
Leaper, S., E. O. Avendaño Cáceres, J. M. Luque-Alled, S. H. Cartmell, and P. Gorgojo (2021). POSS-Functionalized Graphene Oxide/PVDF Electrospun Membranes for Complete Arsenic Removal Using Membrane Distillation. *ACS Applied Polymer Materials*, **3**(4); 1854–1865
Li, M., J. Li, M. Zhou, Y. Xian, Y. Shui, M. Wu, and Y. Yao (2020). Super-Hydrophilic Electrospun PVDF/PVA-Blended Nanofiber Membrane for Microfiltration with Ultrahigh Water Flux. *Journal of Applied Polymer Science*, **137**(9)
Li, N., W. Wang, L. Zhu, W. Cui, X. Chen, B. Zhang, and Z. Zhang (2021). A Novel Electro-Cleanable PAN-ZnO Nanofiber Membrane with Superior Water Flux and Electrocatalytic Properties for Organic Pollutant Degradation. *Chemical Engineering Journal*, **421**; 127857
Liu, K., M. Sorgato, and E. Savio (2025). From Hydrophilic to Superhydrophobic: Tuning Surface Wettability through Salvinia-Inspired Topographies. *ACS Applied Materials & Interfaces*, **17**(31); 45066–45081
Liu, Q., N. Xu, L. Fan, A. Ding, and Q. Dong (2020). Polyacrylonitrile (PAN)/TiO_2 Mixed Matrix Membrane Synthesis by Thermally Induced Self-Crosslinking for Thermal and Organic-Solvent Resistant Filtration. *Chemical Engineering Science*, **228**; 115993
Liu, X., L. Kong, X. Zhao, K. Wu, and Z. Tan (2023). A Method for Alkali Hydrolysis Modification of PAN/PES/-TiO_2 Composite Ultrafiltration Membranes. *Desalination and Water Treatment*, **306**; 165–177
Liu, Z., R. Navik, H. Tan, Q. Xiang, Wahyudiono, M. Goto, and Y. Zhao (2022). Graphene-Based Materials Prepared by Supercritical Fluid Technology and Its Application in Energy Storage. *The Journal of Supercritical Fluids*, **188**; 105672
Manikandan, V. and N. Y. Lee (2023). Reduced Graphene Oxide: Biofabrication and Environmental Applications. *Chemosphere*, **311**; 136934
Mataram, A., A. Firdaus, M. Yanis, R. Dani, S. Nasir, A. F. Ismail, and M. H. D. Othman (2024). Synthesis of Polyethersulfone/Titanium Dioxide Membranes: Analysis of Morphology, Mechanical Properties, and Water Filtration Performance. *Eastern-European Journal of Enterprise Technologies*, **6**(6); 16–25
Mohamat, R., S. A. Bakar, Muqoyyanah, A. Mohamed, S. N. E. A. M. Kamal, M. H. D. Othman, and B. Astuti (2022). Effect of Triple-Tail Surfactant on the Morphological Properties of Polyethersulfone-Based Membrane and Its Antifouling Ability. *Journal of Materials Science*, **57**(34)
Mohd Ali Jinnah, S. N. H., U. F. Md Ali, S. C. Gopinath, N. Ibrahim, R. Ahmad, and F. Mohamed Zuki (2024). Oil Palm Waste-Derived Reduced Graphene Oxide (rGO) for Dynamic Adsorption of Dye in a Fixed-Bed System. *Desalination and Water Treatment*, **317**; 100019
Mokarami, M. S. A. and H. Sereshti (2024). Fabrication of a Green Double-Layered Hybrid Nanocomposite via Electrospinning of Polyethersulphone/Natural Deep Eutectic Solvent on Bacterial Cellulose for Determination of Multiclass Pesticides in Water Samples. *Journal of Chromatography A*, **1735**; 465267
Mokhtari-Shourijeh, Z., S. Langari, L. Montazerghaem, and N. M. Mahmoodi (2020). Synthesis of Porous Aminated PAN/PVDF Composite Nanofibers by Electrospinning: Characterization and Direct Red 23 Removal. *Journal of Environmental Chemical Engineering*, **8**(4); 103876
Motlokoa, T. R., W. K. Maboya, C. Mbileni-Morema, S. J. Modise, and B. J. Okoli (2025). Modification of Polyethersulfone with Partially Reduced Graphene Oxide and Its Water Purification Application. *Desalination and Water Treatment*, **323**; 101341
Mousa, H. M., M. Hamdy, M. A. Yassin, M. M. El-Sayed Seleman, and G. T. Abdel-Jaber (2022). Characterization of Nanofiber Composite Membrane for High Water Flux and Antibacterial Properties. *Colloids and Surfaces A: Physicochemical and Engineering Aspects*, **651**; 129655
Nabila, R., W. Hidayat, A. Haryanto, U. Hasanudin, D. A. Iryani, S. Lee, and J. Yoo (2023). Oil Palm Biomass in Indonesia: Thermochemical Upgrading and Its Utilization. *Renewable and Sustainable Energy Reviews*, **176**; 113193
Pervez, M. N., M. E. Talukder, M. R. Mishu, A. Buonerba, P. del Gaudio, G. K. Stylios, and V. Naddeo (2022). Fabrication of Polyethersulfone/Polyacrylonitrile Electrospun Nanofiber Membrane for Food Industry Wastewater Treatment. *Journal of Water Process Engineering*, **47**; 102838
Qosim, N., G. R. Williams, and M. Edirisinghe (2025). The Tailored Manufacturing of Core (Cellulose Acetate)-Sheath (Polyvinylpyrrolidone) Polymeric Nanofibers for Biphasic Drug Delivery Systems Using Pressure-Spinning. *Materials & Design*, **253**; 113939
Rangecroft, S., R. M. Dextre, I. Richter, C. V. Grados Bueno, C. Kelly, C. Turin, and C. Clason (2023). Unravelling and Understanding Local Perceptions of Water Quality in the Santa Basin, Peru. *Journal of Hydrology*, **625**; 129949
Rapisarda, M., A. Damasco, G. Abbate, and M. Meo (2020). Carbon Black and Reduced Graphene Oxide Nanocomposite for Binder-Free Supercapacitors with Reduced Graphene Oxide Paper as the Current Collector. *ACS Omega*, **5**(50); 32426–32435
Rinovian, A., M. Merita, A. Labanni, S. Sriyono, N. Handayani, M. Amin, and M. Nasir (2025). Synthesis, Characterization, and Fabrication of Linear Nanofiber Structure of Poly(vinylidene Fluoride)/MgO Copolymer via Electrospinning Method. *JOM*, **77**(3); 1367–1375
Ristiani, D., R. Asih, F. Astuti, M. A. Baqiya, C. Kaewhan, S. Tunmee, and Darminto (2022). Mesostructural Study on Graphenic-Based Carbon Prepared from Coconut Shells by Heat Treatment and Liquid Exfoliation. *Heliyon*, **8**(3); e09032
Roche, R. and F. Yalcinkaya (2019). Electrospun Polyacrylonitrile Nanofibrous Membranes for Point-of-Use Water and Air Cleaning. *ChemistryOpen*, **8**(1); 97–103
Rostami, M., G. Jahed-Khaniki, E. M. Aghaee, N. Shariatifar, M. A. Sani, M. Azami, and M. Ghorbani (2024). Poly-

caprolactone/Polyacrylic Acid/Graphene Oxide Composite Nanofibers as a Highly Efficient Sorbent to Remove Lead Toxic Metal from Drinking Water and Apple Juice. *Scientific Reports*, **14**(1)

Sabet, M. and H. Soleimani (2022). Influence of Graphene Oxide on the Mechanical, Thermal and Roughness of Polyethersulphone. *Bulletin of Materials Science*, **45**(1); 1@articleRinovian2025JOM, author = Rinovian, A. and Merita, M. and Labanni, A. and Sriyono, S. and Handayani, N. and Amin, M. and Nasir, M., title = Synthesis, Characterization, and Fabrication of Linear Nanofiber Structure of Poly(vinylidene Fluoride)/MgO Copolymer via Electrospinning Method, journal = JOM, volume = 77, number = 3, pages = 1367–1375, year = 2025, doi = 10.1007/s11837–024–07095–z

Sam, S., S. P. Malinga, and N. Mabuba (2021). Carbon Nanodots Embedded on a Polyethersulfone Membrane for Cadmium(II) Removal from Water. *Membranes*, **11**(2); 1–21

Sarlak, N., M. A. F. Nejad, S. Shakhesi, and K. Shabani (2012). Effects of Electrospinning Parameters on Titanium Dioxide Nanofibers Diameter and Morphology: An Investigation by Box-Wilson Central Composite Design (CCD). *Chemical Engineering Journal*, **210**

Schuepfer, D. B., F. Badaczewski, J. M. Guerra-Castro, D. M. Hofmann, C. Heiliger, B. Smarsly, and P. J. Klar (2020). Assessing the Structural Properties of Graphitic and Non-Graphitic Carbons by Raman Spectroscopy. *Carbon*, **161**; 359–372

Shahryari, Z., M. Yeganeh, K. Gheisari, and B. Ramezanzadeh (2021). A Brief Review of the Graphene Oxide-Based Polymer Nanocomposite Coatings: Preparation, Characterization, and Properties. *Journal of Coatings Technology and Research*, **18**

Sriyanti, I., M. R. Almafie, R. Dani, L. Marlina, L. N. Mulyani, R. S. A. Idjan, and Y. Kurniawati (2026). Optimization of PVP/PCL Nanofiber Diameter Using Coaxial Electrospinning: Response Surface Methodology and Physicochemical Characterization. *South African Journal of Chemical Engineering*, **55**; 298–315

Sriyanti, I., M. R. Almafie, M. K. Nuha Ap Idjan, R. Dani, I. Solihah, E. Syafri, and L. Marlina (2025). Electrospun Nanofiber Membrane of Piper Beetle Loaded PVDF/PAN for Medical Mask Applications: Physicochemical Characteristics, Antibacterial and Air Filter Test. *Advanced Membranes*, **5**; 100149

Sriyanti, I., R. F. Ramadhani, M. R. Almafie, M. K. N. Ap Idjan, E. Syafri, I. Solihah, and A. Fudholi (2024). Physicochemical and Mechanical Properties of Polyvinylidene Fluoride Nanofiber Membranes. *Case Studies in Chemical and Environmental Engineering*, **9**; 100588

Sun, L., Q. Gu, H. Wang, J. Yu, and X. Zhou (2021). Anhydrous Proton Conductivity of Electrospun Phosphoric Acid-Doped PVP-PVDF Nanofibers and Composite Membranes Containing MOF Fillers. *RSC Advances*, **11**(47); 29527–29536

Tohamy, H.-A. S., F. E.-Z. S. Mohamed, and M. El-Sakhawy (2024). Novel Microwave Assisted Carboxymethyl-Graphene Oxide and Its Hepatoprotective Activity. *BMC Pharmacology and Toxicology*, **25**(1); 50

Upadhyay, J., R. Borah, T. M. Das, and J. M. Das (2023). Flexible Solid-State Supercapacitor Based on Ternary Nanocomposites of Reduced Graphene Oxide and Ruthenium Oxide Nanoparticles Bridged by Polyaniline Nanofibers. *Journal of Energy Storage*, **72**

Utkan, G., G. Yumusak, B. C. Tunali, T. Ozturk, and M. Turk (2023). Production of Reduced Graphene Oxide by Using Three Different Microorganisms and Investigation of Their Cell Interactions. *ACS Omega*, **8**(34); 31188–31200

Vali, I. P., B. S. Anusha, M. Pruthvija, S. Savitha, S. Ravindra, M. Nagaveni, and N. Swathi (2024). Bamboo and Coconut Shell Based Activated Carbon: A Raman Spectroscopic Study. *Materials Chemistry and Physics*, **318**; 129240

Vella, D., D. Vengust, P. Umek, A. Rezaei, M. Jezeršek, and A. Mrzel (2025). Efficient Decoration of Graphene Oxide with a Narrow Size Distribution of Noble Metal Nanoparticles: Green Reduction and Integration into a Thermoelastic Composite. *Synthetic Metals*, **313**; 117894

Wang, X., R. Wang, Y. Xu, and G. Wei (2025). Recent Advances in Biohybrid Membranes for Water Treatment: Preparation Strategies, Nano-Hybridization, Bioinspired Functionalization, Applications, and Sustainability Analysis. *Journal of Materials Chemistry A*, **13**(33); 26967–27000

Widiatmoko, P., I. F. Sukmana, I. Nurdin, T. Prakoso, and H. Devianto (2019). Increasing Yield of Graphene Synthesis from Oil Palm Empty Fruit Bunch via Two-Stages Pyrolysis. *IOP Conference Series: Materials Science and Engineering*, **543**(1); 012032

Wu, Z., K. Zheng, G. Zhang, L. Huang, and S. Zhou (2024). Preparation of Polysulfone-Based Nanofiber Janus Membrane for Membrane Distillation Containing Organic Pollutants. *NPJ Clean Water*, **7**(1)

Xue, S., C. Ji, M. D. Kowal, J. C. Molas, C.-W. Lin, B. T. McVerry, and R. B. Kaner (2020). Nanostructured Graphene Oxide Composite Membranes with Ultrapermeability and Mechanical Robustness. *Nano Letters*, **20**(4); 2209–2218

Yang, Y., B. Xie, Q. Liu, B. Kong, and H. Wang (2020). Fabrication and Characterization of a Novel Polysaccharide-Based Composite Nanofiber Films with Tunable Physical Properties. *Carbohydrate Polymers*, **236**; 116054

Yu, J., Y. Mou, Q. Lai, Y. Zhang, C. Di, B. Zhu, and K. Qiao (2024). Facile Construction of Flexible Pitch@PAN Heterojunction Nanofibers with Excellent Conductivity Performance Based on Spontaneous Phase Separation Spinning Technology. *Macromolecules*, **57**(8); 3557–3567

Zakaria, N. Z. J., S. Rozali, N. M. Mubarak, and S. Ibrahim (2024). A Review of the Recent Trend in the Synthesis of Carbon Nanomaterials Derived from Oil Palm By-Product Materials. *Biomass Conversion and Biorefinery*, **14**; 13–44

Zeng, W., M. Yu, J. Lin, L. Huang, J. Li, S. Lin, and L. Chen (2023). Electrospun Chitosan Nanofiber Constructing Superhigh-Water-Flux Forward Osmosis Membrane.

International Journal of Biological Macromolecules, **226**; 833–839

Zhao, D. L., W. Zhou, L. Shen, B. Li, H. Sun, Q. Zeng, and T. S. Chung (2024). New Directions on Membranes for Removal and Degradation of Emerging Pollutants in Aqueous Systems. *Water Research*, **251**; 121111

Zhao, Z., K. Muylaert, and I. F. J. Vankelecom (2021). Combining Patterned Membrane Filtration and Flocculation for Economical Microalgae Harvesting. *Water Research*, **198**; 117181

Zhou, S., Z. Qiu, M. Strømme, and Z. Wang (2020). Highly Crystalline PEDOT Nanofiber Templated by Highly Crystalline Nanocellulose. *Advanced Functional Materials*, **30**(49)

Zulfi, A., S. Hartati, S. Nur'aini, A. Noviyanto, and M. Nasir (2023). Electrospun Nanofibers from Waste Polyvinyl Chloride Loaded Silver and Titanium Dioxide for Water Treatment Applications. *ACS Omega*, **8**(26); 23622–23632